Transformation of dense shelf water cascade into turbidity currents: insights from high-resolution geophysical datasets

Nan Wu[1*], Guangfa Zhong[1], Yakufu Niyazi[2], Biwen Wang[1], Harya D. Nugraha[3], Michael J. Steventon[4]

[1]State Key Laboratory of Marine Geology, Tongji University, 1239 Siping Road, Shanghai, 200092, China

[2]Minderoo-UWA Deep-Sea Research Centre, School of Biological Sciences and UWA Oceans Institute, The University of Western Australia, Perth, WA 6009, Australia

[3]Center for Sustainable Geoscience and Outreach (CSGO), Universitas Pertamina, Jakarta, 12220, Indonesia

[4]Shell Research, Shell Centre, London, SE1 7NA, UK

[*]Email: nanwu@tongji.edu.cn

ABSTRACT

Dense shelf water cascade (DSWC) is a common oceanographic phenomenon on many continental shelves. Previous studies indicate that the DSWC could shape seabed physiography and carry seawater, sediment, and organic carbon a long distance from the continental shelf to the basin floor. However, it remains enigmatic how these DSWC's interact with seabed geomorphology and travel long distances from the shallow to deep marine environments. In this study, we employed high-resolution multibeam bathymetry, 2D and 3D seismic reflection, core description, and sediment grain size data from the Gippsland Basin, southeast offshore Australia. The continental shelf of the central Gippsland Basin stores sediment supplied by the along-shelf transported DSWC. By calculating the sediment motion threshold, we demonstrate that the DSWC is capable of entraining sediment from, and forming dense bottom nepheloid layers above, the seabed. Seismic reflection data reveal that cyclic steps are common on the shelf and slope, indicating a downslope-transported, supercritical current-dominated environment. Core observation and grain size analyses reveal that coarse-grained, Ta-typed turbidites are the major facies, indicating the presence of high-intensity downslope-traversing turbidity currents. Thus, supercritical turbidity currents are the dominant sedimentary process in the central Gippsland Basin. We illuminate that DSWC can interact with pre-existing seabed bathymetry created by a buried submarine landslide, resuspending sediment and igniting downslope-transported turbidity currents. The presence of numerous cyclic steps indicates that the turbidity current can evolve into a supercritical regime upon ignition, leaving complex seabed geomorphology and allowing the forming currents to travel across the shelf and extend more than 80 km down the lower slope. As revealed by our literature review, we imply that the transformation of DSWC into turbidity currents should be a common sedimentary process on outer continental shelves globally, significantly sculpting the seabed morphology and facilitating sediment and other marine particles transportation from shallow to deep sea.

Keywords: Dense shelf water cascade (DSWC), Current transformation, Turbidity-current initiation, Gippsland Basin

1. INTRODUCTION

Along the continental shelves, seasonal evaporation during summer and cooling during winter can generate a cross-shelf density gradient that drives denser seawater transport seawards along the seabed (Ivanov et al., 2004; Canals et al., 2006). This process is defined as a dense shelf water cascade (hereafter DSWC). The DSWC is a climate-driven oceanographic phenomenon prominent throughout the tropical to the high-latitude continental margins (Figure 1A; Ivanov et al., 2004; Amblas and Dowdeswell, 2018; Mahjabin et al., 2020; Gales et al., 2021). The DSWC has been repeatedly measured and well-studied by both long-term and high-frequency in situ measurements in physical oceanography observations (i.e. Canals et al., 2006; Puig et al., 2008; Canals et al., 2009). Once the DSWC is initiated, it sinks and overflows the outer shelf area under the influence of gravity, cascading downslope until it reaches its density equilibrium depth (also known as neutral density level; Figure 1B) (Fohrmann et al., 1998; Canals et al., 2009). Results indicate the DSWC can travel more than 10,000 km along the coastline and descends more than 1000 m down the slope and eventually flooding the basin floor (Figure 1B; Ivanov et al., 2004; Canals et al., 2009; Mahjabin et al., 2020). When transported along the shelf, DSWC can travel at a high speed (i.e. 1.2 m/s) and is highly erosive (Canals et al., 2006; Puig, 2017). For example, the DSWC can dislodge a c. 400 kg anchor at least 3 km away from its mooring position, and polish the rusty iron of the train wheel very shiny through continuous sandblasting associated with the powerful cascading currents (Puig et al., 2008).

The DSWC can affect a large portion of the seabed, induce erosion and deposition, and generate bottom nepheloid layers (zones) that contain significant amounts of suspended sediments and subsequently produce fast travelling gravity flows (Figure 1B; Canals et al., 2006; Puig, 2017). At specific locations, canyons are often the major conduits and determine the paths and spreading conditions for the DSWC (Canals et al., 2006; Morrison et al., 2020; Gales et al., 2021). The DSWC has proved to be an effective seabed-sculpting agent and is capable of transferring large amounts of water and heat, sediments, organic carbon, marine pollutants and nutrients from the shallow marine to the deep ocean (Canals et al., 2006; Puig et al., 2008; Canals et al., 2009). Therefore, the DSWC plays an important role in global deep-ocean circulation, sediment source-to-sink, earth's climate system, and carbon and biogeochemical cycles (Amblas and Dowdeswell, 2018).

Despite the extensive existing literature, some important questions remain to be addressed. Firstly, the process of how DSWC produces gravity flows and shape seabed geomorphology is still poorly understood (Canals et al., 2006; Talling, 2014). Secondly, the reasons for the DSWC spreading over a considerable distance across the shelf and even reaching the lower slope remain unclear. Here we attempt to unravel these important, yet under-explored aspects of DSWC, by presenting observations based on high-resolution bathymetric multibeam, seismic reflection, piston core and sediment grain size datasets from the offshore Gippsland Basin, Australia. The occurrence of the DSWC has brought a large amount of sediment and resulted in extremely complex seabed geomorphology in the central Gippsland Basin (Godfrey et al., 1980; Tomczak, 1985; Mitchell et al., 2007b). The complex seabed geomorphology reflects the action of a range of oceanographic and sedimentary processes at multiple spatiotemporal scales. Therefore, the central region of the Gippsland Basin provides an ideal place to investigate the remaining questions we raised above. We revealed that the DSWC can interact with pre-existing seabed depressions caused by deposited submarine landslide, igniting turbidity currents and leaving erosional bedforms on the seabed. We highlight that the transformation of the DSWC into turbidity currents is an underappreciated sedimentary process that should be common on outer continental shelves globally. The transition from the DSWC to the turbidity current is crucial to understanding the evolution of seabed geomorphology through time, as well as the mechanisms that account for the long-distance transportation of the DSWC under the influence of dynamic oceanographic processes.

2. GEOLOGICAL SETTING

2.1 The Gippsland Basin

The offshore Gippsland Basin is dominated by a cool-water carbonate system located on SE Australia's passive margin, between the mainland of Australia and Tasmania (Figures 2A, 2B; Rahmanian et al., 1990). It is one of Australia's most prolific hydrocarbon provinces, fisheries, and potential carbon storage, and holds a number of other potential marine resource applications (Rahmanian et al., 1990; Mitchell et al., 2007a; Mitchell et al., 2007b). The Gippsland Basin belongs to a series of rift basins formed along the southern margin of the Australian plate, due to the separation of Antarctica and Australian continents during the breakup of Gondwana in the Mesozoic (Colwell et al., 1993). Since the Pleistocene, the Gippsland Basin has been detached from major river sources, allowing the development of a cool water carbonate province with minimal terrigenous input (Mitchell et al., 2007b). The margin of the Gippsland Basin is dominated by a c. 100 km wide embayment, and the SE margin of the basin is floored by c. 120 km long and 15-70 km wide, ESE-trending Bass Canyon system (Figures 2A, 2B).

2.2 Climate and oceanography

The Bass Strait is a shallow (water depth range from 40-60 m) coastal sea between mainland Australia and Tasmania, connecting the Great Australian Bight in the west and the Tasman Sea in the east (Figure 2A; Tomczak, 1985; Lavering, 1994). In winter, the shallow Bass Strait imposes a limit on the penetration of thermal convection, and as a consequence, Bass Strait seawater cools rapidly and has a higher salinity than that of the surface layer in the Tasman Sea (Lavering, 1994). Therefore, when seawater leaves the Bass Strait on its eastern side, it has a prominent density contrast against the Tasman Sea water (Tomczak, 1985). As a consequence, cold, denser Bass Strait seawater can flow into and sink beneath the warmer, fresher water of the Gippsland shelf, generating the northeast-flowing Bass Cascade Current (hereafter BCC) which sinks to the 200-400 m isobaths and extends more than tens of kilometres (Figure 2B; Godfrey et al., 1980; Li et al., 2005; Mitchell et al., 2007b). Observations from the ocean bottom stations have revealed that the BCC is the densest seawater offshore SE Australia, it is active every year and is with an average transport rate of 1.0 Sverdrups (Sv; 1Sv=10^6 m^3/s) (Middleton and Bye, 2007). The transportation of BCC has transported significant quantities of water and sediments and spread along the shelf edge over a long distance (Boland, 1971). For example, distinctive temperature-salinity anomalies are found at 200-800 m depth in the Tasman Sea, most likely caused by Bass Strait seawater penetration (Figure 2C; Boland, 1971). In the Gippsland Basin, the central continental shelf is dominated by the Westerly wind throughout the year (especially in winter; Figure 2B; Li et al., 2005). The eastward-flowing Westerly wind flows at 10-30 km/h with maximum gusts reaching 100 km/h. Therefore, the Westerly wind has created a moderate to high energy wave-dominated environment and a robust NE-transported Ekman Transport Flow (ETF) in a water depth of c. 200-300 m (Figure 2B; Mitchell et al., 2007a; O'Brien et al., 2018). The East Australia Current (EAC) is a western boundary current that carries warm equatorial waters and flows southward adjacent to Australia's southeast coast (Figure 2B, 2D). It is up to 500 m deep and 100 km wide, occasionally extending far enough south to reverse the movement of water in the Gippsland Basin during summer months (Li et al., 2005). Therefore, the combination of seasonal northward flowing BCC, the southward flowing EAC, and northeast flowing ETF have jointly controlled the oceanography and sedimentation along SE Australia's continental margin.

3. DATASET AND METHODOLOGY

The datasets available for this study include multibeam bathymetry data with a coverage area of c. 250,000 km^2, 2D and 3D seismic reflection data with a coverage area of c. 1700 km^2, with lithology control provided by six-piston core samples (Figures 2B, 3A).

3.1 Multibeam bathymetry

Multibeam bathymetry data for this study is sourced from Geoscience Australia's Marine data portal (http://marine.ga.gov.au). The dataset is compiled from multiple bathymetric surveys and gridded at 50x50 m; hence, geomorphological features smaller than 50 m across cannot be differentiated. The multibeam bathymetry dataset covers the Gippsland Basin continental shelf, at around 200 m water depth, to the Tasman Sea Abyssal plain, at over 4000 m water depth (Figure 3A).

3.2 Seismic data

We adopt two types of seismic reflection data provided by Geoscience Australia (http://www.ga.gov.au/nopims): (i) A 2D regional seismic section which is up to c. 90 km long, therefore providing excellent coverage from Gippsland Basin shelf region to Bass Canyon abyssal plain (Figure 3C); and (ii) two 3D seismic reflection surveys (Elver 3D and Tuskfish 3D), which covered an area of c. 650 km^2 and 1050 km^2, respectively (Figure 2B). Both 3D seismic datasets are post-stack time-migrated and zero-phase processed, and a downward decrease and increase in acoustic impedance are expressed as blue (negative) and red (positive) seismic reflections, respectively. The

3D seismic surveys have a dominant frequency content of 70 hertz and an average seismic velocity of 1700 m/s near the seabed sediment, which gives an approximate vertical resolution of c. 6 m for the near seabed sediments. The 3D seismic resolution is therefore sufficient to map the geometry of detailed seabed sedimentary and structural features. We further extract the dip illumination seismic attribute (see Appendix S1 for an explanation), from the 3D seismic dataset to determine the seabed geometries and geomorphology of the interpreted submarine deposits.

3.3 Piston Core and grain Size

Comprehensive sediment sampling and piston cores collection was conducted from RV Franklin cruise in 1998 (FR11/98) (Exon et al., 2002). In this study, we adopted six-piston cores in the continental shelf and slope areas over a water depth range of 200-2500 m. The detailed core descriptions and interpretations are compiled from (Mitchell et al., 2007b), which have provided lithological and sedimentary facies constraints for the study area. In addition, we analyzed seabed grain size distribution data from 13 locations, obtained from the Geoscience Australia Marine Sediment Database (https://portal.ga.gov.au). For the purpose of this current research, we analyzed the proportion of mud (<65 µm), sand (between 65 µm and 2 mm) and gravel (> 2mm) within each sampling locations.

3.4 Sediment incipient motion calculation

To determine whether BCC can entrain and suspend sediments during transportation, we calculate the critical condition for sediment incipient motion using the method proposed by Soulsby (1997). Soulsby (1997) equations resolve critical seabed shear stress (τ_{cr}) and bottom shear stress due to currents (τ_b), if $\tau_b<\tau_{cr}$, the seabed sediments are immobile (i.e. no movement), if $\tau_b>\tau_{cr}$, the seabed sediments are mobile and can be suspended and transported (Soulsby, 1997). In continental shelf settings, Soulsby (1997) method is widely applied and has been proven effective for quantifying the threshold of sediment motion under marine current environments (i.e. Villacieros-Robineau et al., 2019).

The τ_{cr} of seabed composed mainly of cohesive sediments was calculated using Equations (1) - (3) from Soulsby (1997).

$$\tau_{cr} = g\theta_{cr}(\rho_s - \rho_w)d \tag{1}$$

$$\theta_{cr} = 0.3 \,/\, (1 + 1.2D_*) + 0.055(1 - e^{-0.02D_*}) \tag{2}$$

$$D_* = [g(\rho_S - \rho_w) \,/\, (\rho_w v^2)]^{1/3} d \tag{3}$$

where g is gravitational acceleration, 9.81 m/s^2; ρ_s is sediment density, 2,650 kg/m^3; ρ_w is current density of BCC, 1,023.2 kg/m^3 according to Tomczak (1987); d is sediment grain size, ranging from 65 μm to 2 mm on the continental shelf of Gippsland Basin; θ_{cr} is critical Shields parameter; D_* is dimensionless grain size parameter; v is kinematic viscosity for seawater, 1.212 × 10^{-6} m^2/s at 35 salinity and 15 °C (Luick et al., 1994).

The bottom shear stress τ_b and the shear velocity u^* impacted by currents are calculated via the law of the wall, using Equations (4) - (5):

$$u^* = kU(z) / \mathrm{Ln}(z / z_0) \quad (4)$$

$$\tau_b = u^{*2}\rho_w \quad (5)$$

where $U(z)$ is the current velocity measured at a depth of z meter above the seabed, we adopt 20 m of z and chose a current speed of 0.5–1.0 m/s as measured by Acoustic Doppler Current Profiler (Luick et al., 1994); k is von Kármán constant, 0.40$\pm$0.02 (Bailey et al., 2014); z_0 is reference height related to the seabed, for muddy seabed is estimated to be c. 0.2 mm (Soulsby, 1983).

4. RESULT

We divide the Gippsland Basin into Northern, Central, and Southern regions based on geographical position and seabed morphology (Figures 3A, 3B). The continental shelf of the Central region extends seaward for approximately 70 km with an average dip of 0.8^o then abruptly steepens to 8.8^o in the slope (Figure 3C). The water depth of the Central region ranges from 0-500 m on the shelf and from 500-2000 m on the slope (Figure 3A). Below we describe the seabed geomorphology and the major sedimentary environments from the shelf to the slope in the Central region of the Gippsland Basin.

4.1 Seabed geomorphology of the shelf area

Observation: The Central region is characterized by an erosional seabed (Figures 4A, 4B). On the shelf, a set of north-trending scallop-shaped scarps have been observed near the outer shelf area (Figure 4C). Seismic sections indicate the scallop-shaped scarps show a clear truncation edge and erosional base surface (termed as basal shear surface), marking the boundary that differentiates the overlying deformed strata from the undeformed sediments (Figures 5A, 5B). Downslope (eastward) to the scarps, a series of sediment wave fields have been observed along the middle part of the outer shelf (Figure 4B, 4C). Further downslope, the sediment waves are dissected by a set of irregular discontinuous concave-downslope scours that occur at the southwestern part of the shelf (Figures 4B, 4C). In the seismic section, the scours range from 1.2-1.7 km in width, 1.7-5 km in length (spacing), from 80-150 m in depth, and with an aspect ratio (wavelength/height) from 28-53 (Figure 5C). These scours are normally characterized by truncated, steep lee sides and gentle, slightly upslope-dipping stoss sides (Figure 5C). Buried step-like bedforms are observed beneath seabed scours (see insert figure in Figure 5C). The buried bedforms contain sub-parallel, relatively high-amplitude seismic reflections, and show upslope migration by erosion in the lee side and deposition in the stoss side (Figure 5C).

Further NE, three sets of scours aligned in distinctive or discontinuous channel-shaped depressions have been observed in the centre part of the shelf (Figure 4C). The crests of these scours are consistently oriented approximately north-south, being confined in the axis of channel-shaped morphology (Figure 4C). Seismic sections cutting along the thalweg of the channel-shaped depressions show a series of bedforms that form a train of steps and stretch over a distance of 10-16 km (Figures 5D, 5E). These bedforms range from 0.2-0.7 km in width, 0.6-1.1 km in wavelength, 30-98 m in wave height, and with aspect ratio from 18-30 (Figures 5D, 5E). A single bedform is characterized by a steep scarp indicated by truncated seismic reflections that form the lee side contrast with a gently, lower relief slope at the stoss side (Figures 5D, 5E).

Further NE of the shelf, at least two well-developed channels have been observed in the eastern part of the shelf (Figure 4C). Nevertheless, these channels only extend to the shelf break, and no clear erosions have been observed within the slope (Figures 4B, 4C). These channels vary from 2–10 km in width, and 100–325 m in depth (Figure 4B). They initially trend SSE and then sharply divert to the NE within a few kilometres distance across the shelf break, and ultimately run to the slope after passing through the shelf break (Figures 4B, 4C). A set of longitudinal lineations has been observed on the southern flank of the channels (Figure 4C). These lineations are c. 8 km long, they are evenly spaced and predominantly oriented parallel to the channel axis. In the seismic section, the longitudinal lineations show a stair-shaped cross-sectional geometry and truncations (Figure 5F).

Interpretation: The scalloped scarps developed near the outer shelf indicate a gradual broadening over time is likely caused by slope failures (i.e. Lee and Chough, 2001). The scalloped scarps are thus interpreted as headwall scarps associated with a buried landslide (Figures 5A, 5B). The scours, scour trains, and channels are developed above the landslide’s basal shear surface, suggesting the landslide is being deposited and predates these bedforms (Figures 5C-F). The sediment wave fields developed within the scarps are evident in the presence of downslope currents (i.e. Fildani et al., 2006). The asymmetrical cross-sectional geometry, large aspect ratio, and upslope migration trend indicate the scours are erosional cyclic steps (or cyclic scours) that are carved by downslope flowing supercritical currents (Figure 5C; Fildani et al., 2006; Kostic, 2011). Scours aligned within the channel template are interpreted as erosional cyclic step trains, which may indicate an incipient channel formation (i.e. Taki and Parker, 2005; Fildani et al., 2006; Fildani et al., 2013; Zhong et al., 2015). The buried step-like bedforms are interpreted as partially depositional cyclic steps, formed when sediment erosion on the lee side is less than sediment deposition on the stoss side (Slootman and Cartigny, 2020). The presence of the partially depositional cyclic steps suggests that the downslope flowing currents were active in the Central region for an extended period of time.

The channel's diversion near the shelf edge could be a result of the Westerly wind-induced Ekman transport flow (ETF), which follows a NE-NNE direction, interacting with the sedimentary systems along the edge of the continental shelf (Mitchell et al., 2007a). The EAC is less likely to contribute to the deviation of the channel axis, as it separates from the coast approximately between 30°S and 32°S, splitting into eddy-dominated southern and eastern extensions (Cetina-Heredia et al., 2014; Oke et al., 2019). The major eddies are anticlockwise, and therefore, the channel courses should be diverted to the southeast direction, which is opposite to our observation.

The longitudinal lineations developed within the channels are interpreted as sedimentary furrows similar to those observed in other submarine settings (i.e. Wynn and Stow, 2002; Puig et al., 2008). Studies of furrows show that these features were formed due to recurring, stable, and directional currents (i.e. turbidity currents) erosion through time (e.g. Flood, 1983; Puig et al., 2008). The presence of furrows in this study suggests that the ambient downslope flowing currents may have strong and persistent energy (Flood, 1983). The sole appearance of furrows on the channel's southern flank suggests that the downslope flowing currents preferential arrival across the southern channel flank.

4.2 Seabed geomorphology of the slope area

Observation: Near the upper slope, gullies and landslide scarps are widely distributed on the slope between water depths 700 to 2000 m (Figure 6). The gullies extend several kilometres from the upper slope to the lower slope, terminating as the slope angle decreases and intersects with the Bass Canyon head (Figures 4B, 6). The gullies are straight and oriented to the dip direction of the slope, characterized by linear morphology, rounded heads and narrow bodies in plain view (Figure 6). Small failures and slide scarps are evident within or around the edges of the gullies. In the seismic section, these gullies are V-shaped, and have a relatively flat base reflection with clear erosive truncation along the sidewalls (Figure 7A). The gully sidewalls have a relief (incision depth) of 110-230 m, and a width of 120-280 m (Figure 7A). The landslide scarps roughly dip from NNE to SSW, with widths ranging from c. 4 km to 7km (Figure

6). In seismic sections, these scarps show a stair-shape, backward (i.e. landward) dipping geometry (Figure 7B).

Near the lower slope, scours that are aligned in train and parallel to the slope dip direction have been observed within the gullies and on the inter-gully ridges (Figure 6). Seismic sections cutting along the thalweg of the scour trains show that they are characterized by steep and erosional lee sides and gentle stoss sides, similar to the cyclic steps developed on the shelf (Figures 7B-D). These scours are 0.58-1.3 km in wavelength, 48-154 m in wave height, and aspect ratio is from 7-30. They are best developed near the lower slope, where the slope gradient drops from 9^{o}-12^{o} (near the upper slope) to 4^{o}-7^{o} (to the lower slope; Figures 7B-D). Further lower slope, giant landslide scarps that distribute more than 30 km horizontally are observed near the lowermost of the slope (Figure 6). In the seismic section, the scarps show clear truncations that separate the undeformed seabed (upslope) from the deformed erosional seabed (downslope) (Figures 7B-D).

Interpretation: Near the upper slope, the step-shaped pattern of the scarps suggests a retrogressive failure mechanism of the landslides (Figure 7B; Wu et al., 2021). As the landslide is located along the shelf edge, where cyclic wave loading can constantly rework seabed sediments. This process may account for a potential trigger mechanism leading to slope failure (i.e. Marshall et al., 1978; Bea et al., 1983). The gullies clearly incise into the landslides, suggesting that they post-date the slope failures (Figure 6).

The linear gullies are interpreted as the conduits for gravity flows to transport sediment to deeper waters (Micallef and Mountjoy, 2011; Lonergan et al., 2013). The V-shaped head geometry indicates the origin of the gullies is associated with downslope gravity-driven currents (i.e. debris flow and turbidity current; Farre et al., 1983; Gales et al., 2012). Successive small failures are exhibited on the gully ridges, which is indicative of a gradual widening of the gullies (Post et al., 2022). The scour trains developed within the gullies and on the inter-gully ridges are interpreted as cyclic steps, similar to their counterparts developed on the shelf (i.e. Fildani et al., 2006). The presence of cyclic steps suggests that the slope area is also a supercritical flow regime-dominated environment, and the erosion by supercritical currents might play a role in the gully's initiation and evolution (i.e. Noormets et al., 2009; Gales et al., 2012).

Our observation suggests that cyclic steps are scarce on the upper slope, where the slope gradient is steeper (9°-12°), but prominent on the lower slope, where the slope gradient is relatively gentle (4°-7°) (Figures 7B-D). The discrepancy of the cyclic steps on the upper slope can be explained as the higher slope gradient can cause the overflowing currents to have a faster velocity, thereby suppressing their ability to decelerate and undergo internal hydraulic jumps (Kostic, 2011; Zhong et al., 2015). Due to the higher flow velocity (therefore more energetic), erosional scours and truncations are common on the upper slope (Figures 7C, 7D). Further downslope, cyclic steps preferentially form near the lower slope area (Figures 7B-D), suggesting the transition from high slope gradients to low slope gradients could promote the formation of the cyclic steps (i.e. Covault et al., 2017; Fildani et al., 2021). The construction of cyclic steps has led to the formation of local high topographies near the distal side of the lower slope (Figures 7B-D). These local topographic highs can form 12^{o}-22^{o} slopes and range from 70-130 m high, leaving a series of spatially evacuated accommodations near the distal edge of the lower slope (Figures 7B-D). These evacuated accommodations can reduce the lower slope's lateral confining pressure, thus increasing seabed instability (Bull et al., 2009). This can be evidenced by the giant submarine landslides occurring immediately adjacent to, and continuous headwall scarps developing near the distal side of the local topographic highs (Figures 7B-D). Therefore, we indicate that the local topographic highs can act as landslide-susceptible structures that ultimately prime slope failures.

4.3 Piston core and grain size analysis

Observation: Facies-1 can be observed from the shelf and slope (core #1-4 and 6; Figure 4B). On the shelf, Facies-1 are observed within the headwall scarps of the buried submarine landslide (Figure 4B). Facies-1 is normally graded, moderately to well-sorted, and contains coarse-grained sand (predominately near the lower part) with a sharp top surface and an erosional base surface (Figure 8A). Facies-1 collected from the slope area suggests this facies is internally structureless and contains shelf-restricted bioclasts (core #4 and 6; Figure 4B). Facies-2 can be observed from the upper-lower slope (core #5 and 6; Figure 4B). Facies-2 contains sand- and silt-sized bioclasts, quartz and siliciclastic clay. Core observation indicates it is poorly sorted, matrix-supported and often organic-rich (Figure 8B). It also has decimetre-thick bedding with gradational contacts with bioturbation observed (Figure 8B).

There are significant differences in grain size distributions between sediment samples collected outside (west) and within (east) the headwall scarps associated with the buried landslide (Figure 8C). Sediment samples collected upslope (west) of the headwall scarps show fine-to-medium sand grain size, and the predominant particle diameter is between 65 μm and 2 mm (Figure 8C). In comparison, sediment sample collected within the headwall scarps exhibits sharp grain size variations (Figure 8C). Specifically, the sediment has an average particle diameter exceeding 2 mm and consists primarily of coarse-grained gravel.

Interpretation: The erosional base surface, coarse-grained, normally graded, and internally structureless nature of Facies-1 is a typical indicator of Bouma Ta-typed turbidites, which are primarily formed by downslope transported turbidity currents (Bouma, 1962). The abundance of shelf-restricted bioclasts observed from the slope suggests these turbidites originated from the shelf. Therefore, we interpret Facies-1 as turbidites formed by turbidity currents sourced from the continental shelf. The fine-grained and organic-rich nature of Facies-2 suggests it is deposited under a low energy condition. We interpret Facies-2 as representing the background slope environment (Mitchell et al., 2007b).

BCC is the dominant oceanographic process on the shelf of the central Gippsland Basin (Mitchell et al., 2007b), considering the minimum (c. 0.5 m/s) and maximum (c. 1.0 m/s) speed of the BCC (Luick et al., 1994), the sediment grain size that is smaller than 639 μm and 2.036 mm would be motional, respectively (Figure 8D). The BCC is therefore capable of entraining most sediment calibres from the seabed (Figure 8C) and of forming dense, bottom nepheloid layers during transportation, as suggested by previous monitoring studies (i.e. Godfrey et al., 1986). The sudden increase in grain size collected within the headwall scarps suggests a highly turbulent and energetic flow that is capable of carrying coarse-grained sediments is active (Postma and Cartigny, 2014). Core analyses conducted in the same area indicate this highly turbulent and energetic flow is downslope transported turbidity current. Thus, the significant change in grain size may be attributed to the transition from along-shelf transported BCC to downslope transported turbidity current, and the transformation process occurs adjacent to the headwall scarps of the buried landslide.

5. DISCUSSION

5.1 Turbidity current: the dominant sedimentary process in central Gippsland Basin

The seismic interpretations reveal a continued presence of cyclic steps throughout the outer shelf and slope areas (Figures 4C and 6), which indicate a continuing role of downslope-transported supercritical currents in sculpting and remoulding the seabed. Published studies suggest that the overriding flow that creates cyclic steps is supercritical turbidity currents with alternating transformation between supercritical and subcritical flow through hydraulic jumps (i.e. Zhong et al., 2015; Covault et al., 2017; Fildani et al., 2021). Core observation and grain size analyses have confirmed this interpretation, as coarse-grained, Ta-typed turbidites are the major facies, indicating the presence of high-intensity downslope-traversing turbidity currents (Figures 8A, 8C; Bouma, 1962). Additionally, recent publications indicate that Ta-typed turbidites can be formed by hydraulic jump-related rapid sedimentation, often associated with high-energy supercritical turbidity currents (Figure 8A; i.e. Postma and Cartigny, 2014). Therefore, by combining the results from seismic interpretation, core observation, and grain size analyses, we interpret that turbidity currents are an important sedimentary process in the central Gippsland Basin.

5.2 The initiation of turbidity current: transformation from the dense shelf water cascade

The origin of turbidity currents has been attributed to three main processes, transformation from the slope failures, hyperpycnal flows from onshore fluvial input or subglacial meltwater, and oceanographic processes generated flows near the shelf edge (Piper and Normark, 2009; Talling et al., 2013). In Gippsland Basin, the Central region has been completely disconnected from onshore drainage systems since the Pleistocene (Mitchell et al., 2007b), and no modern submarine landslides (only buried landslide; Figure 5B) are observed in the central shelf. Therefore, slope failures and onshore fluvial input cannot contribute to the initiation of turbidity currents.

Oceanographic processes including storms, tides, and internal waves may play a role in resuspending seabed sediments and igniting episodic flows. Nevertheless, as they occur periodically in most cirmuestances and their influence is often multi-directional, they thus lack the ability to generate recurring and stable currents. This contrasts with our observations, where the erosional features developed on the shelf are inferred to reflect a recurring, directionally stable flow that is sufficiently strong to erode the seabed (i.e. Figures 4C, 5C-F). BCC is the primary oceanographic process active on the shelf of the Central Gippsland Basin (Mitchell et al., 2007b), and it could be a reasonable cause of turbidity currents. The following sections will examine the processes involved in this current transformation and investigate how turbidity currents can be maintained during transportation.

As BCC propagates along and cascades across the continental shelf of the Gippsland Basin, the sediment entraining process has allowed a density contrast near the bottom of the BCC from the surrounding seawater, forming dense, bottom nepheloid layers that hover above the seabed (Figures 9A, 9B; Godfrey et al., 1980; Mitchell et al., 2007b). An equilibrium condition could have remained when BCC flows within a relatively smooth and flat (c. 0.8^{o}) shelf region, until it flows into the area affected by the pre-existing submarine landslide. The headwall scarps of the landslide are 40-70 m deep and are characterized by a steep gradient (7^{o}-10^{o}), which has caused local seabed depressions and slope gradient variation (Figures 9B, 9C). When the bottom nepheloid layer moves across and flows over these headwall scarps, a sudden increase in slope gradient could breach the flow equilibrium condition and enhance the shear stress (thus entraining capacity) and flow velocity (Ogston et al., 2008; Traer et al., 2012; Traer et al., 2018). Consequently, the headwall scarps can cause the dense nepheloid layers to split and sink (Figure 9C). The denser layer would subsequently hover over the seabed and potentially accelerate when traversing the scarps (Figure 9C). Accelerating flows could cause additional perturbations and entrain more sediment, and ultimately ignite a turbidity current (Figure 9C; i.e. Parker et al., 1986; Ogston et al., 2008). The headwall scarps on the shelf extend over 70 km along the BCC's transport direction (Figures 3A and 9A), which allows the above-mentioned process to continue and sediments to remain suspended as the BCC moves. As sediments are continuously resuspended, they serve as a recurrent source of turbidity current ignition. In summary, we indicate that on the continental shelf, the submarine landslide emplacement first, then the BCC opportunistically uses the headwall scarps as a 'perturbation point' to transform into turbidity currents and lock in place for subsequent erosional processes (i.e. the formation of cyclic steps; Figure 9A). Other oscillatory oceanographic processes, including Westerly wind-generated strong wave actions and storm-generated currents, may coincide with the BCC (or act as external forces to enhance the BCC) and simultaneously resuspend large amounts of seabed unconsolidated sediments and generate downslope flows, potentially contributing to the initiation of turbidity currents (Figure 9D; Micallef and Mountjoy, 2011; Talling et al., 2013).

After ignition, the steep gradient (7°-10°) of the headwall scarps would provide ample opportunity for turbidity currents to evolve into the Froude supercritical regime (Figure 9C). Piper et al. (1999) demonstrate a similar process in the Grand Banks, where a 6° scarp can facilitate debris flow to transform into supercritical turbidity currents. During transportation, the hydraulic jumps could strengthen flow turbulence by producing large-scale eddies and standing waves within the turbidity current and promote the erosional process (Traer et al., 2012; Hiscott et al., 2013). The steep slope can also facilitate the flow acceleration and resulting increased shear stress (i.e. Eqs. 4 and 5), potentially forming lateral confinement (i.e. levee) of the flows and increasing flow erosional forces (Rowland et al., 2010). The presence of 10-16 km-long cyclic step trains suggests that the turbidity currents have high flow intensity and can repeatedly shape the seabed (Figure 4C). Additionally, the aspect ratio of cyclic steps shows a decreasing trend from the shelf to the slope, suggesting that the formative flow energy can increase when entering the steep slope (Figure 8E; Nakajima and Satoh, 2001). Therefore, we indicate that the ignited turbidity currents are unlikely to settle from suspension and have strong energy to transport downslope for a long distance.

5.3 When and where does this transformation occur?

The study area is not the only place where such current transformation occurs, similar diagnostics have been found in the SW Adriatic margin and the NW Mediterranean Seas. The DSWCs in these two places can also entrain seabed sediment and form bottom-dense nepheloid layers, and therefore, potentially initiate turbidity currents (see Appendix 3 for quantification details). In the SW Adriatic margin, where DSWC flows into Gondola Slide's headwall scarp region, the DSWC creates an area of extreme seabed complexity characterised by several large-scale scours aligned in a channel template (cf. Figure 7 of Canals et al., 2009). In the Bari Canyon system, Trincardi et al. (2007) proved that when intense DSWC flows through the canyon head, it can be captured, confined, and transported in a flow regime similar to that of a turbidity current. In the NW Mediterranean Seas, when DSWC cascades into and channelizing through the head of the Cap de Creus Canyon, it carries coarse particles and forms field of giant furrows and overconsolidated the substrate mud (Puig et al., 2008; Puig, 2017). Additionally, when DSWC cascades into the canyon heads of the Bourcart Canyon, the current accelerates and transports coarser particles than before entering the canyon head (Gaudin et al., 2006). All the seabed geomorphologies and erosive features identified in the above-mentioned studies require directional, stable and highly energetic processes to develop. Although the published works interpret these erosional features as being formed by the DSWC (Canals et al., 2006; Puig et al., 2008), it is highly reasonable that the DSWC interacted with the pre-existing seabed topographies and transformed into a turbidity current before creating these erosional bedforms. The transformed turbidity current thus carries coarse material and abrades the seabed, induces resuspension and generates erosive bedforms.

Therefore, we note that the transformation of the DSWC into turbidity currents should be a common process on the outer continental shelves globally. We infer that this current transformation can occur where the seabed gradient has a sharp increase, usually caused by the presence of faults and folds associated with submarine landslides and/or canyons. The newly transformed turbidity currents are competent to establish erosional conditions and become sufficiently large and energetic to carry coarse-grained sediments to reach the lower slope and even the basin floor. Additionally, this current transformation has unravelled the puzzle for the long-distance transportation ability of the DSWC, since turbidity currents can often extend hundreds of kilometres and constitute a significant mechanism for sediment transfer from shallow to deep marine settings (i.e. Pirmez and Imran, 2003).

5.4 The evolution of seabed geomorphology

Cyclic steps and related supercritical bedforms are recognised as fundamentally important building blocks of seabed geomorphology evolution in many submarine settings (Fildani et al., 2006; Covault et al., 2017; Fildani et al., 2021). On the shelf of Gippsland Basin, the presence of scour, scour trains, and developed channels reveals a time-step channel maturation stage in a natural submarine setting (i.e. Figure 4C). This maturation of channel forms resembles and proves the cartoon model established in previous studies, which depicts the ideal stages of channel development (cf. Figure 7 of Fildani et al., 2013; Fildani et al., 2021). In the Gippsland Basin, the scour and scour trains can represent morphodynamic signals for turbidity current channel initiation (Figure 4C; Fildani et al., 2013). The scours can help to focus the subsequent turbidity currents and cause the scours to coalesce, creating an erosional template for the development of a new channel (Fildani et al., 2013). The scour trains can represent morphodynamic signals for turbidity current channel initiation (Figure 4C; Fildani et al., 2013). Under the continuous erosion associated with turbidity currents, these scour trains could migrate upslope and gradually become a developed channel (Fildani et al., 2013). The channel could further evolve laterally and longitudinally, ultimately forming a mature submarine drainage network (i.e. canyon) under the maintenance of sediment capture associated with turbidity currents.

On the slope of Gippsland Basin, the supercritical turbidity currents have resulted in considerable seabed erosion, generating widespread gullies that represent an immature drainage system (Figures 10A, 10B; Santangelo et al., 2013). With the continuous downslope transportation of the turbidity currents and other gravity flows (i.e. submarine landslides), the gullies will act as preferential conduits for large-scale sediment transfer and may ultimately evolve into submarine canyons (Figure 10C; Santangelo et al., 2013).

6. CONCLUSION

Our results elucidate the dense shelf water cascade (DSWC) can interact with pre-existing submarine landslides and subsequently transform into (supercritical) turbidity currents. The newly transformed turbidity currents are an effective seabed sculpting tool and hugely influenced the modern seabed geomorphology and sedimentation process. We infer that this current transformation can occur where the seabed gradient has a sharp increase, usually caused by the presence of faults and folds associated with submarine landslides and/or canyons. As DSWC is prominent on many continental margins, we suggest that this current transformation represents an unappreciated, yet important trigger for turbidity currents on the outer continental shelves globally. In 2022, the Australian Government announced new wind farm construction plans in the Gippsland Basin (the same area as this study; see from Victorian State Government website). As turbidity currents can be hazardous to submarine infrastructures (Carter et al., 2014), we suggest that future marine spatial planning and offshore constructions should consider a 20-40 km wide (the width of the BCC) band of the buffer zone landward to the landslide headwall scarps located on the central shelf (Figure 10C).

FIGURE CAPTIONS

Figure 1. (A) Occurrence previously documented dense shelf water cascade (DSWC) around the world. Numbers in each area refer to the location: (1) Eastern Chukchi Sea shelf, (2) Beaufort Sea shelf, (3) Foxe Basin, northernmost part of Hudson Bay, (4) SW Greenland margin, (5) Northern gulf of California, (6) North American south-eastern shelf, (7) Great Bahama Bank, (8) East Greenland Shelf and south of Denmark Strait, (9) West Spitsbergen shelf, (10) Bear Island Channel, Barents Sea, (11) hindered in Storfjord, Barents Sea, (12) Skagerrak, eastern flank of the North Sea, (13) Rockall Bank, North Atlantic Ocean, (14) Celtic Sea shelf, North Atlantic Ocean, (15) Gulf of Lion, NW Mediterranean Sea, (16) Gondola slide area, Adriatic Sea shelf, (17) Cape Bari, SE Adriatic Sea shelf, (18) Southern Mediterranean Sea shelf, (19) Aegean Sea shelf, (20) Banc d'Arguin, near Cape Blanc and off the west African coast, (21) Western shelf of Novaya Zemlya, Barents Sea, (22) shelf of Nansen Basin, Arctic Ocean, (23) North-eastern Severnaya Zemlya shelf, Laptev Sea, (24) Northern sea of Okhotsk, north-western Pacific Ocean, (25) Peter the Great Bay, near the Japan Sea continental slope, (26) NW Australia inner shelf, (27) Shark Bay, western Australia, (28) Great Australian Bight, southern Australia, (29) Jervis Bay, southern Australia, (30) Bass Strait, south-eastern Australia, (31) Spencer Gulf, east Australia, (32) The Hikurangi subduction margin, SE of central New Zealand, (33) The western Ross Sea, Antarctic Ocean, (34) The Adélie Coast, East Antarctic sector, Antarctic Ocean, (35) Prydz Bay, East Antarctica, (36) Southern margin of Weddell Sea shelf, (37) Eastern margin of Weddell Sea shelf, (38) The southern Ross Sea, Antarctic Ocean. Note that the blue dots are based on the

DSWC global atlas by Ivanov et al. (2004) and the DSWC recorded around Australian shelves by Mahjabin et al. (2020). The pink dots indicate recently reported (2004–present) cascading phenomena measured by long-term and high-frequency in situ measurements globally, see Appendix 2 for the supporting references. (B) Schematics of the DSWC mechanism showing the formation of intermediate nepheloid layers on the shelf and the downslope turbidity currents. Adapted from Fohrmann et al. (1998).

Figure 2. (A) The regional map of Australia shows the location of the study area (indicated in a red polygon) and the oceanographic setting. The trajectories of the main oceanic currents are represented by white, blue, and yellow dashed lines. LC, Leeuwin Current; SAC, South Australian Current; ZC, Zeehan Current; BCC, Bass Cascade Current; EAC, East Australian Current. In Gippsland Basin, when the BCC flows through the Bass Strait during winter, it is further fed by the LC, ZC and the wind stress within the Bass Strait, jointly transporting Bass Strait water towards the front (Li et al., 2005; Mitchell et al., 2007b). During summer, though the BCC is less active, strong offshore wind and tidal activities can further reinforce and transport Bass Strait water eastwards (Godfrey et al., 1980). (B) Zoom in view of the Gippsland Basin and the Bass Canyon. Note the north arrow (white) and the yellow box denote the location of the 3D seismic data. The transportation pathway of the BCC is based on data collected from the Conductivity, Temperature, and Depth (CTD) sensors adopted during the winter of 1981 by Tomczak (1985). The transportation pathway of the EAC is adopted from Lavering (1994) and Ridgway and Hill (2009). (C) Temperature profile of the Bass Strait

showing the downward temperature anomalies within the continental shelf and slope. (D) Temperature profile (potential temperature) in offshore eastern Australia, showing the depth of the East Australian Current (EAC). The temperature data is from the WOCE (World Ocean Current Experiment) Hydrographic Program (available at https://odv.awi.de/data/ocean). See Figure 2A for locations.

Figure 3. (A) 3D view of seabed multibeam bathymetric map of the offshore Gippsland Basin and Bass Canyon system, showing the main geomorphologic features. (B) Sketch of Figure 3A, showing the key depositional elements, canyons and distinguished regional domains. (C) Shelf-to-slope seismic profile showing the Central shelf and slope regions. See Figure 3B for location.

Figure 4. (A) Seabed structure map generated from the 3D seismic data, showing the seabed morphology in the Central Region. (B) Dip illumination attribute map calculated from the 3D seismic data, showing the detailed sedimentary structures of the Central Region. Note the yellow dots indicate the piston core location. (C) Zoomed-in view of the continental shelf in the Central Region, emphasizing the sediment waves, cyclic steps and channels. See Figure 4B for location.

Figure 5. (A) Seismic dip section cut through the headwall scarps of the landslide. (B) Interpreted seismic section of Figure 5A. (C) Seismic longitudinal profile along the axis of the cyclic step train. (D) Seismic longitudinal profile cutting through the axis of

channel-formed cyclic steps. The inserted schematic map shows a series of idealized asymmetrical cyclic steps and hypothetical densiometric Froude number (Fr) variability. Within a single bedform, the supercritical flow creates a hydraulic jump (Frd>1) at the base of the lee side and transfers to subcritical flow (Frd<1) at the stoss side. Subsequently, the subcritical flow reaccelerates to supercritical flow again down to the lee side of the next bedform. The schematic map was modified by Cartigny et al. (2011). (E) Seismic longitudinal profile cutting through the axis of channel-formed cyclic steps. (F) Seismic cross-sectional profile cutting through the channels; note the stair-shaped erosional characteristics of furrows developed on the channel sidewalls. See Figure 4C for locations.

Figure 6. Zoomed-in view of the continental slope in the Central Region, emphasizing the landslides and gullies. See Figure 4B for location.

Figure 7. (A) Seismic section illustrating gullies' cross-sectional geometries. (B) Seismic dip section cutting along the gully ridge. (C) Seismic dip section cutting along the gully ridge. (D) Seismic dip section cutting within the gully and along its thalweg. See Figure 6 for locations.

Figure 8. (A) Core sketch generated based on piston core report from the central region of the Gippsland Basin, showing the cross-section of the Facies-1. (B) Core sketch generated based on piston core report, showing the cross-section of Facies-2. Core

locations in Figure 4B. (C) Grain size distribution in the Central area of the Gippsland Basin. The blue arrow indicates the transport direction of the BCC. (D) The sediment motion threshold curve under the given values of sediment grain size and BCC current speed. (E) The relationship between dimensionless aspect ratio (wavelength/height) and slope gradient for cyclic steps in this work and in the literature. Modified from (Slootman and Cartigny, 2020).

Figure 9. (A) The 3D view of the Central Region, showing the seabed morphological structures and major current pathways. (B) Schematic 2D plain view of the Central shelf, illustrating the location of headwall scarps, the pathway of the BCC and its associated supercritical turbidity currents. See Figure 9A for location. (C) Schematic cross-section showing the transformation from BCC to turbidity currents. See the text for explanations and Figure 9B for location. (D) Schematic cross-section depicting the combined influence of the Westerly Wind, internal waves, and tide-induced sediment resuspension and turbidity current initiation. See Figure 9A for location.

Figure 10. Schematic of seabed geomorphology evolution processes in the Central Region of the Gippsland Basin. (A) Shelf: the transformation of the Bass Cascading Current (BCC) into turbidity currents; Slope: the generation of scarps caused by wave activities near the upper slope. (B) Shelf: The formation of the sedimentary structures caused turbidity currents; Slope: The initiation of gullies and the formation of the landslides on the upper slope. (C) Shelf: The evolution from cyclic steps into channels and canyons; Slope: landslide initiation near the lower slope. Note that the buffer zone

indicates a stable seabed not influenced by the current transformation process or the ignited turbidity current.

REFERENCE

Bouma, A.H.P.H.K.F.P.S., 1962. Sedimentology of some Flysch deposits : a graphic approach to facies interpretation. Elsevier, Amsterdam

Boland, F., 1971. Temperature-salinity anomalies at depths between 200m and 800m in the Tasman sea. Marine and Freshwater Research 22, 55-62.

Marshall, N., Stanley, D., Kelling, G., 1978. Large storm-induced sediment slump reopens an unknown Scripps submarine canyon tributary. Sedimentation in submarine canyons, fans, and trenches: Stroudsburg, Pennsylvania, Hutchinson and Ross, 73-84.

Godfrey, J., Jones, I., Maxwell, G., Scott, B., 1980. On the winter cascade from Bass Strait into the Tasman Sea. Marine and Freshwater Research 31, 275-286.

Bea, R.G., Wright, S.G., Sircar, P., Niedoroda, A.W., 1983. Wave-induced slides in south pass block 70, Mississippi Delta. Journal of Geotechnical Engineering 109, 619-644.

Farre, J.A., McGregor, B.A., Ryan, W.B., Robb, J.M., 1983. Breaching the shelfbreak: passage from youthful to mature phase in submarine canyon evolution.

Flood, R.D., 1983. Classification of sedimentary furrows and a model for furrow initiation and evolution. Geological Society of America Bulletin 94, 630-639.

Soulsby, R.L., 1983. The bottom boundary layer of shelf seas, Elsevier oceanography series. Elsevier, pp. 189-266.

Tomczak, 1985. The Bass Strait water cascade during winter 1981. Continental Shelf Research 4, 255-278.

Godfrey, J., Vaudrey, D., Hahn, S., 1986. Observations of the shelf-edge current south of Australia, winter 1982. Journal of Physical Oceanography 16, 668-679.

Parker, G., Fukushima, Y., Pantin, H.M., 1986. Self-accelerating turbidity currents. Journal of Fluid Mechanics 171, 145-181.

Tomczak, M., 1987. The Bass Strait water cascade during summer 1981–1982. Continental Shelf Research 7, 561-572.

Rahmanian, V., Moore, P., Mudge, W., Spring, D., 1990. Sequence stratigraphy and the habitat of hydrocarbons, Gippsland Basin, Australia. Geological Society, London, Special Publications 50, 525-544.

Colwell, J.B., Constantine, A.E., Willcox, J.B., 1993. Regional structure of the Gippsland Basin: interpretation and mapping of a deep seismic data set. Australian Geological Survey Organisation.

Lavering, I.H., 1994. Marine environments of Southeast Australia (Gippsland Shelf and Bass Strait) and the impact of offshore petroleum exploration and production activity. Marine georesources & geotechnology 12, 201-226.

Luick, J.L., Ka, R., Tomczak, M., 1994. On the formation and spreading of the Bass Strait cascade. Continental Shelf Research 14, 385-399.

Soulsby, R., 1997. Dynamics of marine sands.

Fohrmann, H., Backhaus, J.O., Blaume, F., Rumohr, J., 1998. Sediments in bottom-arrested gravity plumes: Numerical case studies. Journal of Physical Oceanography 28, 2250-2274.

Piper, D.J., Cochonat, P., Morrison, M.L., 1999. The sequence of events around the epicentre of the 1929 Grand Banks earthquake: initiation of debris flows and turbidity current inferred from sidescan sonar. Sedimentology 46, 79-97.

Lee, S., Chough, S., 2001. High‐resolution (2–7 kHz) acoustic and geometric characters of submarine creep deposits in the South Korea Plateau, East Sea. Sedimentology 48, 629-644.

Nakajima, T., Satoh, M., 2001. The formation of large mudwaves by turbidity currents on the levees of the Toyama deep‐sea channel, Japan Sea. Sedimentology 48, 435-463.

Exon, N., Hill, P., Partridge, A., Chaproniere, G., Keene, J., 2002. Cretaceous volcanogenic and Miocene calcareous strata dredged from the deepwater Gippsland Basin on RV Franklin

Research Cruise FR11/98. Geoscience Australia Record 7.

Wynn, R.B., Stow, D.A., 2002. Recognition and interpretation of deep-water sediment waves-implications for palaeoceanography, hydrocarbon exploration and flow process interpretation (Introduction to special issue). Marine Geology 192, 1-3.

Pirmez, C., Imran, J., 2003. Reconstruction of turbidity currents in Amazon Channel. Marine and petroleum geology 20, 823-849.

Ivanov, V., Shapiro, G., Huthnance, J., Aleynik, D., Golovin, P., 2004. Cascades of dense water around the world ocean. Progress in oceanography 60, 47-98.

Li, F., Dyt, C., Griffiths, C., Jenkins, C., Rutherford, M., Chittleborough, J., 2005. Seabed sediment transport and offshore pipeline risks in the Australian southeast. The APPEA Journal 45, 523-534.

Taki, K., Parker, G., 2005. Transportational cyclic steps created by flow over an erodible bed. Part 1. Experiments. Journal of Hydraulic Research 43, 488-501.

Canals, M., Puig, P., de Madron, X.D., Heussner, S., Palanques, A., Fabres, J., 2006. Flushing submarine canyons. Nature 444, 354-357.

Fildani, A., Normark, W.R., Kostic, S., Parker, G., 2006. Channel formation by flow stripping: Large-scale scour features along the Monterey East Channel and their relation to sediment waves. Sedimentology 53, 1265-1287.

Gaudin, M., Berné, S., Jouanneau, J.-M., Palanques, A., Puig, P., Mulder, T., Cirac, P., Rabineau, M., Imbert, P., 2006. Massive sand beds attributed to deposition by dense water cascades in the Bourcart canyon head, Gulf of Lions (northwestern Mediterranean Sea). Marine Geology 234, 111-128.

Middleton, J.F., Bye, J.A., 2007. A review of the shelf-slope circulation along Australia's southern shelves: Cape Leeuwin to Portland. Progress in Oceanography 75, 1-41.

Mitchell, J., Holdgate, G., Wallace, M., 2007a. Pliocene–Pleistocene history of the Gippsland Basin outer shelf and canyon heads, southeast Australia. Australian Journal of Earth Sciences 54, 49-64.

Mitchell, J., Holdgate, G., Wallace, M., Gallagher, S., 2007b. Marine geology of the Quaternary Bass Canyon system, southeast Australia: a cool-water carbonate system. Marine geology 237, 71-96.

Trincardi, F., Foglini, F., Verdicchio, G., Asioli, A., Correggiari, A., Minisini, D., Piva, A., Remia, A., Ridente, D., Taviani, M., 2007. The impact of cascading currents on the Bari Canyon System, SW-Adriatic margin (Central Mediterranean). Marine Geology 246, 208-230.

Ogston, A.S., Drexler, T.M., Puig, P., 2008. Sediment delivery, resuspension, and transport in two contrasting canyon environments in the southwest Gulf of Lions. Continental Shelf Research 28, 2000-2016.

Puig, P., Palanques, A., Orange, D., Lastras, G., Canals, M., 2008. Dense shelf water cascades and sedimentary furrow formation in the Cap de Creus Canyon, northwestern Mediterranean Sea. Continental Shelf Research 28, 2017-2030.

Bull, S., Cartwright, J., Huuse, M., 2009. A subsurface evacuation model for submarine slope failure. Basin Research 21, 433-443.

Canals, M., Danovaro, R., Heussner, S., Lykousis, V., Puig, P., Trincardi, F., Calafat, A.M., de Madron, X.D., Palanques, A., Sanchez-Vidal, A., 2009. Cascades in Mediterranean submarine grand canyons. Oceanography 22, 26-43.

Noormets, R., Dowdeswell, J., Larter, R.D., Cofaigh, C.Ó., Evans, J., 2009. Morphology of the upper continental slope in the Bellingshausen and Amundsen Seas–Implications for sedimentary processes at the shelf edge of West Antarctica. Marine Geology 258, 100-114.

Piper, D.J., Normark, W.R., 2009. Processes that initiate turbidity currents and their influence on turbidites: a marine geology perspective. Journal of Sedimentary Research 79, 347-362.

Ridgway, K., Hill, K., 2009. The East Australian Current.

Rowland, J.C., Hilley, G.E., Fildani, A., 2010. A test of initiation of submarine leveed channels by deposition alone. Journal of Sedimentary Research 80, 710-727.

Cartigny, M.J., Postma, G., Van den Berg, J.H., Mastbergen, D.R., 2011. A comparative study of sediment waves and cyclic steps based on geometries, internal structures and numerical modeling. Marine Geology 280, 40-56.

Kostic, S., 2011. Modeling of submarine cyclic steps: Controls on their formation, migration, and architecture. Geosphere 7, 294-304.

Micallef, A., Mountjoy, J.J., 2011. A topographic signature of a hydrodynamic origin for submarine gullies. Geology 39, 115-118.

Gales, J., Larter, R., Mitchell, N., Hillenbrand, C.D., Østerhus, S., Shoosmith, D., 2012. Southern Weddell Sea shelf edge geomorphology: Implications for gully formation by the overflow of high‐salinity water. Journal of Geophysical Research: Earth Surface 117.

Traer, M., Hilley, G., Fildani, A., McHargue, T., 2012. The sensitivity of turbidity currents to mass and momentum exchanges between these underflows and their surroundings. Journal of Geophysical Research: Earth Surface 117.

Fildani, A., Hubbard, S.M., Covault, J.A., Maier, K.L., Romans, B.W., Traer, M., Rowland, J.C., 2013. Erosion at inception of deep-sea channels. Marine and Petroleum Geology 41, 48-61.

Hiscott, R.N., Aksu, A.E., Flood, R.D., Kostylev, V., Yaşar, D., 2013. Widespread overspill from a saline density‐current channel and its interaction with topography on the south‐west Black Sea shelf. Sedimentology 60, 1639-1667.

Lonergan, L., Jamin, N.H., Jackson, C.A.-L., Johnson, H.D., 2013. U-shaped slope gully systems and sediment waves on the passive margin of Gabon (West Africa). Marine Geology 337, 80-97.

Santangelo, M., Gioia, D., Cardinali, M., Guzzetti, F., Schiattarella, M., 2013. Interplay between mass movement and fluvial network organization: An example from southern Apennines, Italy. Geomorphology 188, 54-67.

Talling, P.J., Paull, C.K., Piper, D.J., 2013. How are subaqueous sediment density flows triggered, what is their internal structure and how does it evolve? Direct observations from monitoring of active flows. Earth-Science Reviews 125, 244-287.

Bailey, S.C., Vallikivi, M., Hultmark, M., Smits, A., 2014. Estimating the value of von Kármán's constant in turbulent pipe flow. Journal of Fluid Mechanics 749, 79-98.

Carter, L., Gavey, R., Talling, P.J., Liu, J.T., 2014. Insights into submarine geohazards from breaks in subsea telecommunication cables. Oceanography 27, 58-67.

Cetina‐Heredia, P., Roughan, M., Van Sebille, E., Coleman, M., 2014. Long‐term trends in the East Australian Current separation latitude and eddy driven transport. Journal of Geophysical Research: Oceans 119, 4351-4366.

Postma, G., Cartigny, M.J., 2014. Supercritical and subcritical turbidity currents and their deposits—A synthesis. Geology 42, 987-990.

Talling, P.J., 2014. On the triggers, resulting flow types and frequencies of subaqueous sediment density flows in different settings. Marine Geology 352, 155-182.

Zhong, G., Cartigny, M.J., Kuang, Z., Wang, L., 2015. Cyclic steps along the South Taiwan Shoal and West Penghu submarine canyons on the northeastern continental slope of the South China Sea. Bulletin 127, 804-824.

Covault, J.A., Kostic, S., Paull, C.K., Sylvester, Z., Fildani, A., 2017. Cyclic steps and related supercritical bedforms: building blocks of deep-water depositional systems, western North America. Marine Geology 393, 4-20.

Puig, P., 2017. Dense shelf water cascading and associated bedforms, Atlas of bedforms in the western mediterranean. Springer, pp. 35-40.

Amblas, D., Dowdeswell, J., 2018. Physiographic influences on dense shelf-water cascading down the Antarctic continental slope. Earth-Science Reviews 185, 887-900.

O'Brien, P., Mitchell, C., Nguyen, D., Langford, R., 2018. Mass Transport Complexes on a Cenozoic paleo-shelf edge, Gippsland basin, southeastern Australia. Marine and Petroleum

Geology 98, 783-801.
Traer, M., Fildani, A., Fringer, O., McHargue, T., Hilley, G., 2018. Turbidity current dynamics: 2. Simulating flow evolution toward equilibrium in idealized channels. Journal of Geophysical Research: Earth Surface 123, 520-534.
Oke, P.R., Roughan, M., Cetina-Heredia, P., Pilo, G.S., Ridgway, K.R., Rykova, T., Archer, M.R., Coleman, R.C., Kerry, C.G., Rocha, C., 2019. Revisiting the circulation of the East Australian Current: Its path, separation, and eddy field. Progress in Oceanography 176, 102139.
Villacieros-Robineau, N., Zúñiga, D., Barreiro-González, B., Alonso-Pérez, F., de la Granda, F., Froján, M., Collins, C.A., Barton, E.D., Castro, C.G., 2019. Bottom boundary layer and particle dynamics in an upwelling affected continental margin (NW Iberia). Journal of Geophysical Research: Oceans 124, 9531-9552.
Mahjabin, T., Pattiaratchi, C., Hetzel, Y., 2020. Occurrence and seasonal variability of Dense Shelf Water Cascades along Australian continental shelves. Scientific reports 10, 1-13.
Morrison, A., Hogg, A.M., England, M.H., Spence, P., 2020. Warm Circumpolar Deep Water transport toward Antarctica driven by local dense water export in canyons. Science advances 6, eaav2516.
Slootman, A., Cartigny, M.J., 2020. Cyclic steps: Review and aggradation-based classification. Earth-Science Reviews 201, 102949.
Fildani, A., Kostic, S., Covault, J.A., Maier, K.L., Caress, D.W., Paull, C.K., 2021. Exploring a new breadth of cyclic steps on distal submarine fans. Sedimentology 68, 1378-1399.
Gales, J., Rebesco, M., De Santis, L., Bergamasco, A., Colleoni, F., Kim, S., Accettella, D., Kovacevic, V., Liu, Y., Olivo, E., 2021. Role of dense shelf water in the development of Antarctic submarine canyon morphology. Geomorphology 372, 107453.
Wu, N., Nugraha, H.D., Zhong, F.G., Steventon, M., 2021. The role of mass-transport complexes (MTCs) in the initiation and evolution of submarine canyons.
Post, A.L., Przeslawski, R., Nanson, R., Siwabessy, J., Smith, D., Kirkendale, L.A., Wilson, N.G., 2022. Modern dynamics, morphology and habitats of slope-confined canyons on the northwest Australian margin. Marine Geology 443, 106694.

Figure 1

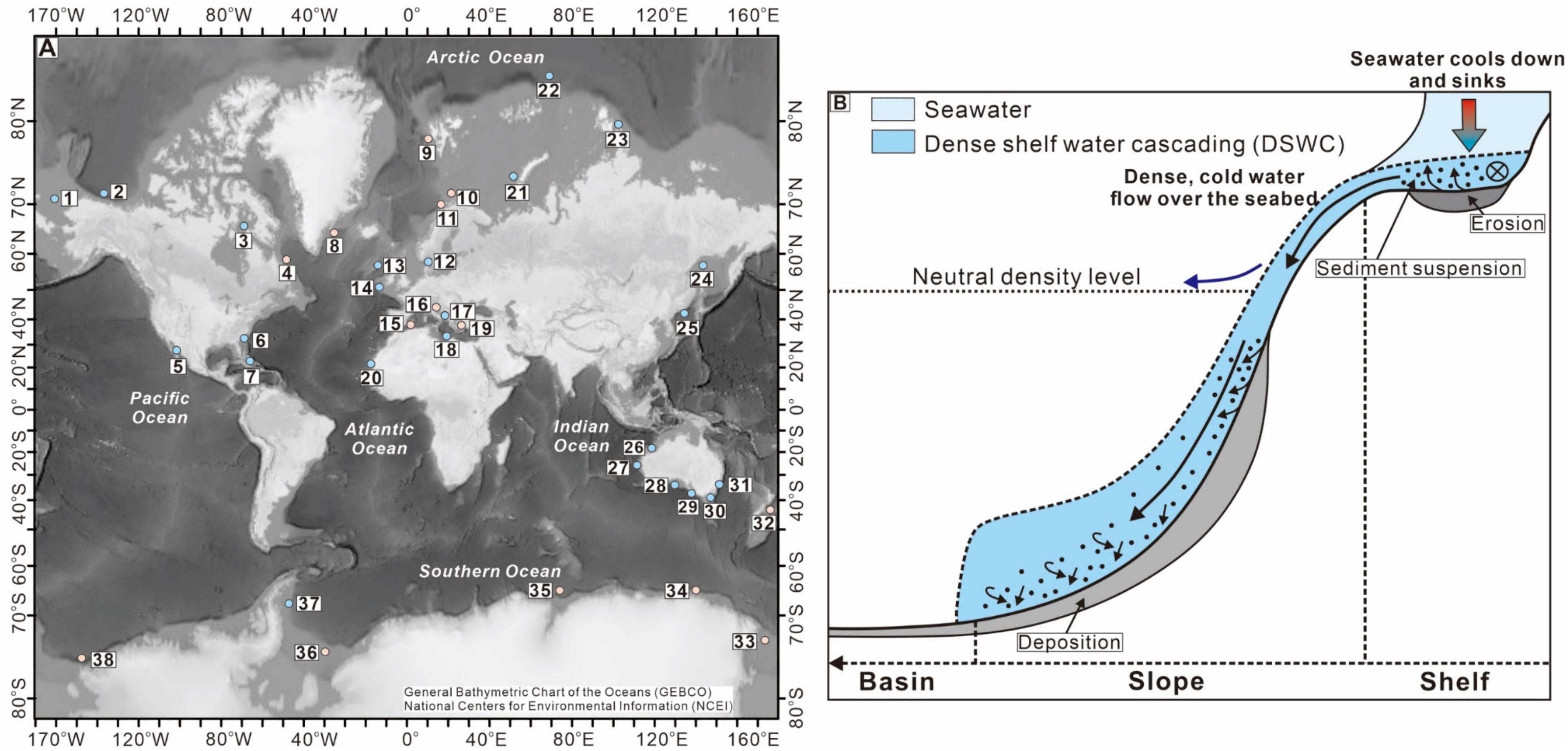
A
Arctic Ocean
Pacific Ocean
Atlantic Ocean
Indian Ocean
Southern Ocean
General Bathymetric Chart of the Oceans (GEBCO)
National Centers for Environmental Information (NCEI)
B
Seawater
Dense shelf water cascading (DSWC)
Seawater cools down and sinks
Dense, cold water flow over the seabed
Erosion
Sediment suspension
Neutral density level
Deposition
Basin
Slope
Shelf

Figure 2

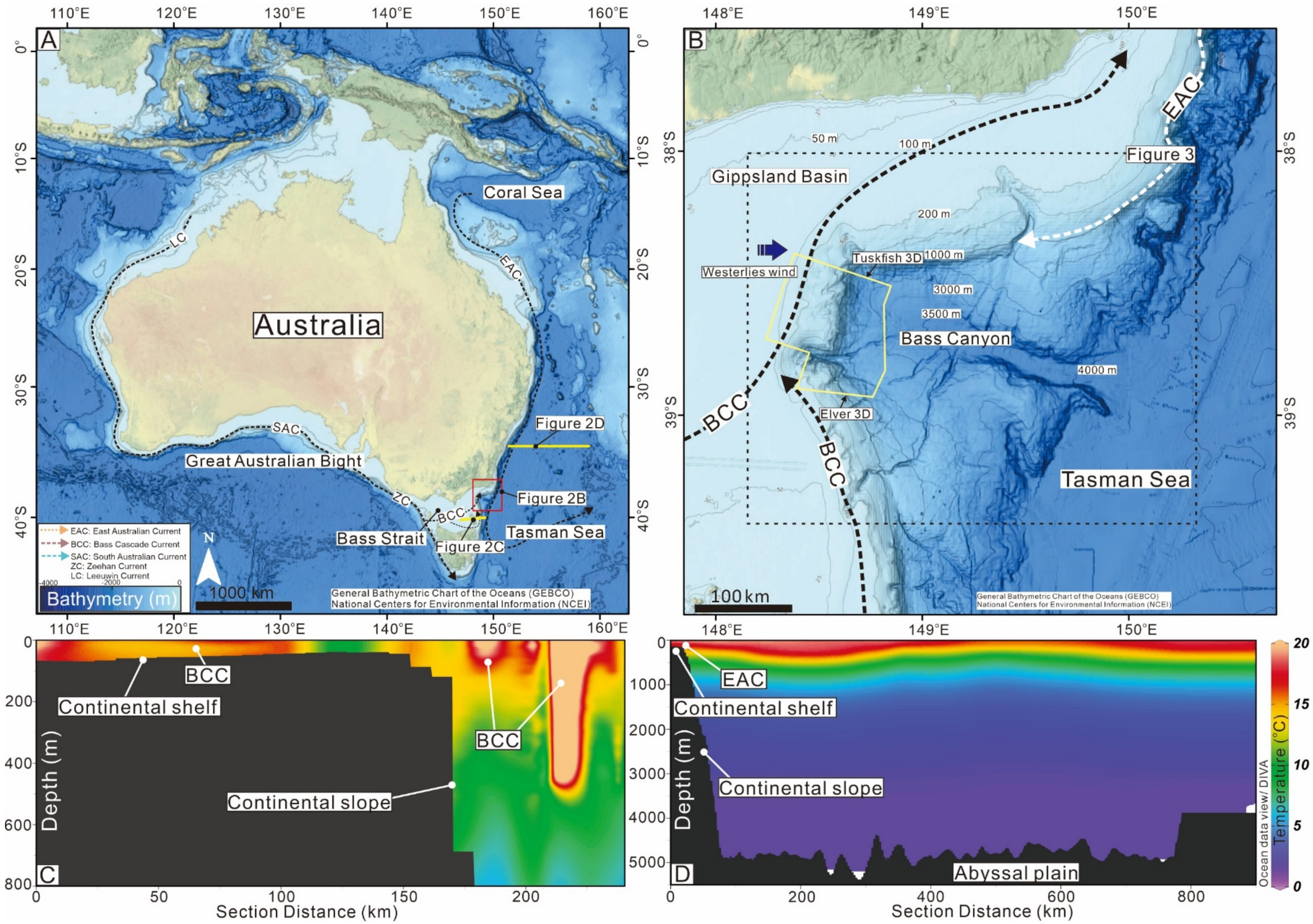
A
Australia
Coral Sea
LC
EAC
SAC
Great Australian Bight
ZC
BCC
Bass Strait
Tasman Sea
Figure 2D
Figure 2B
Figure 2C
EAC: East Australian Current
BCC: Bass Cascade Current
SAC: South Australian Current
ZC: Zeehan Current
LC: Leeuwin Current
Bathymetry (m)
1000 km
General Bathymetric Chart of the Oceans (GEBCO)
National Centers for Environmental Information (NCEI)
B
Gippsland Basin
Westerlies wind
Tuskfish 3D
Elver 3D
Bass Canyon
Tasman Sea
Figure 3
EAC
BCC
50 m
100 m
200 m
1000 m
3000 m
3500 m
4000 m
100 km
C
Continental shelf
BCC
Continental slope
Depth (m)
Section Distance (km)
D
EAC
Continental shelf
Continental slope
Abyssal plain
Depth (m)
Section Distance (km)
Ocean data view/ DIVA
Temperature (°C)

Figure 3

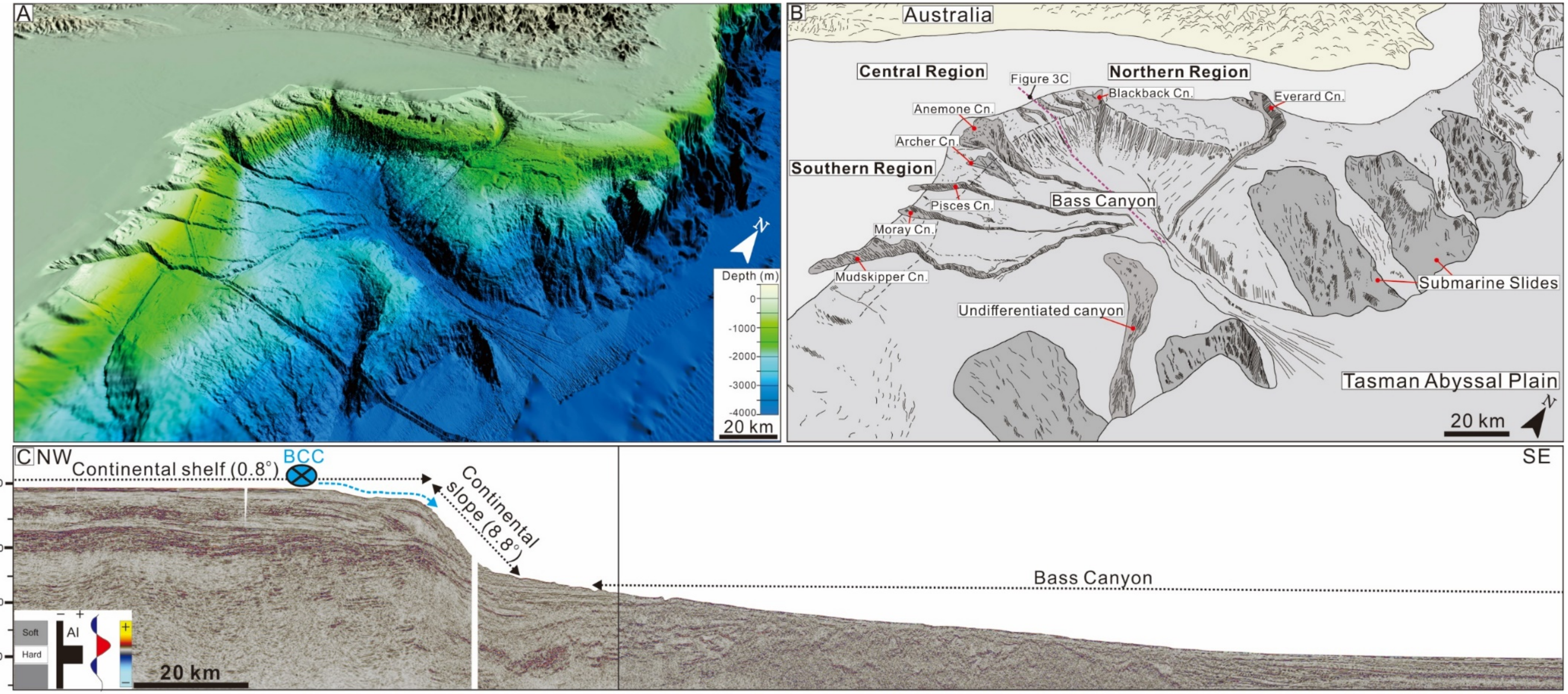
A
Depth (m)
0
-1000
-2000
-3000
-4000
20 km
N
B
Australia
Central Region
Northern Region
Figure 3C
Blackback Cn.
Everard Cn.
Anemone Cn.
Archer Cn.
Southern Region
Bass Canyon
Pisces Cn.
Moray Cn.
Mudskipper Cn.
Submarine Slides
Undifferentiated canyon
Tasman Abyssal Plain
20 km
N
C
NW
Continental shelf (0.8°)
BCC
Continental slope (8.8°)
SE
Bass Canyon
TWT (ms)
0
-2000
-4000
-6000
Soft
Hard
AI
20 km

Figure 4

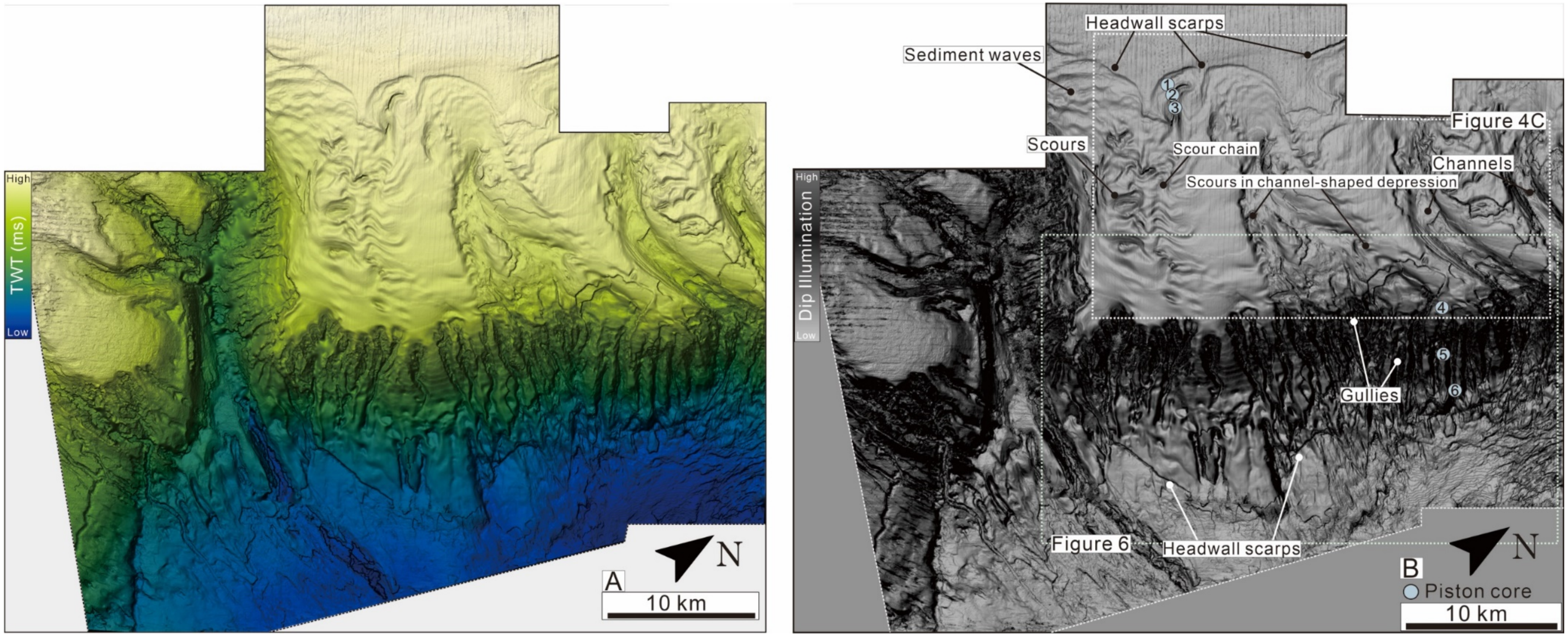
High
TWT (ms)
Low
A
N
10 km
Headwall scarps
Sediment waves
1
2
3
Figure 4C
Scours
Scour chain
Channels
Scours in channel-shaped depression
High
Dip Illumination
Low
4
5
Gullies
6
Figure 6
Headwall scarps
B
N
Piston core
10 km

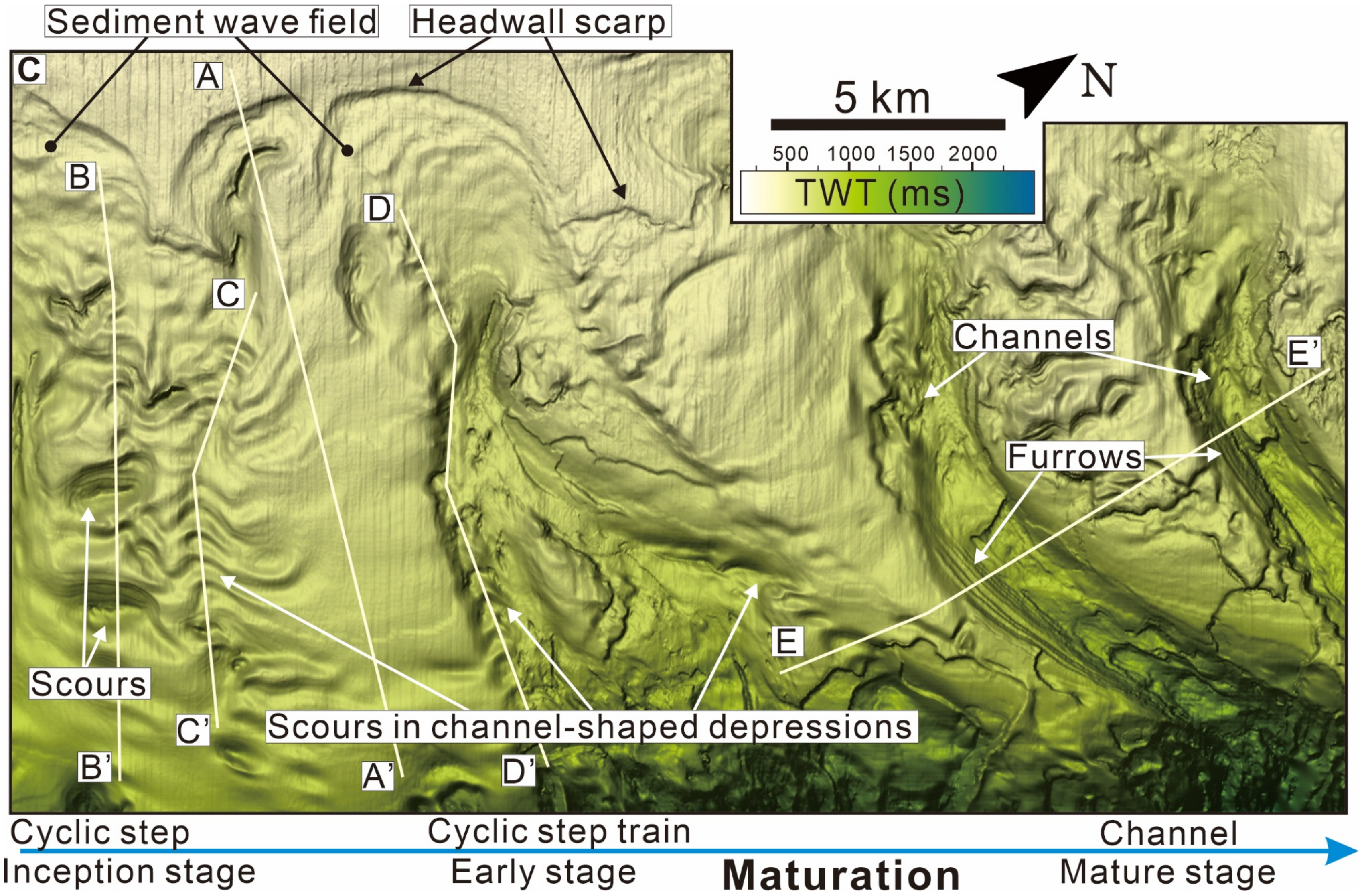
Sediment wave field
Headwall scarp
C
A
B
D
C
5 km
N
500 1000 1500 2000
TWT (ms)
Channels
E'
Furrows
E
Scours
C'
B'
A'
D'
Scours in channel-shaped depressions
Cyclic step
Inception stage
Cyclic step train
Early stage
Maturation
Channel
Mature stage

Figure 5

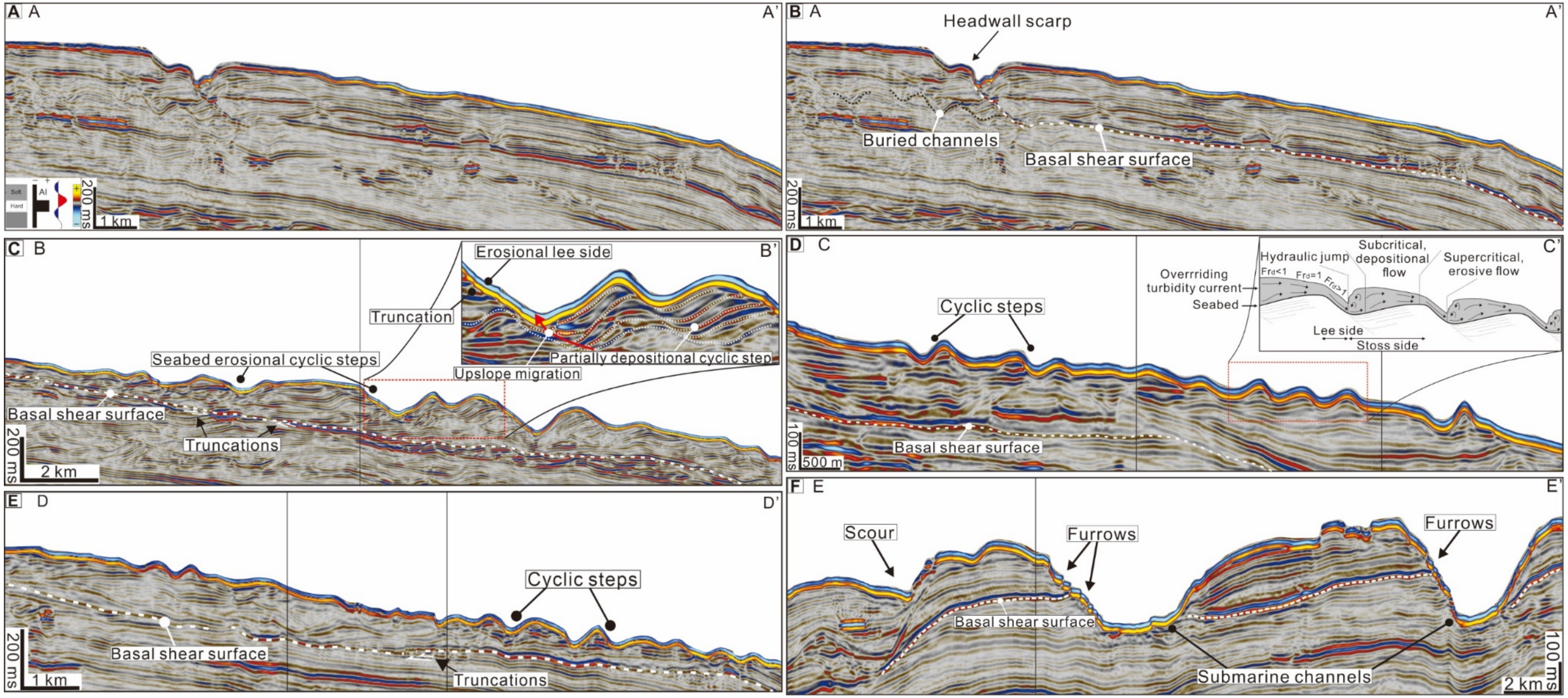

A
A
A'
Soft
Hard
AI
200 ms
1 km
B
A
A'
Headwall scarp
Buried channels
Basal shear surface
200 ms
1 km
C
B
B'
Erosional lee side
Truncation
Seabed erosional cyclic steps
Partially depositional cyclic step
Upslope migration
Basal shear surface
Truncations
200 ms
2 km
D
C
C'
Cyclic steps
Hydraulic jump
Subcritical, depositional flow
Supercritical, erosive flow
Overrriding turbidity current
Seabed
Lee side
Stoss side
Basal shear surface
100 ms
500 m
E
D
D'
Cyclic steps
Basal shear surface
Truncations
200 ms
1 km
F
E
E'
Scour
Furrows
Furrows
Basal shear surface
Submarine channels
100 ms
2 km

Figure 6

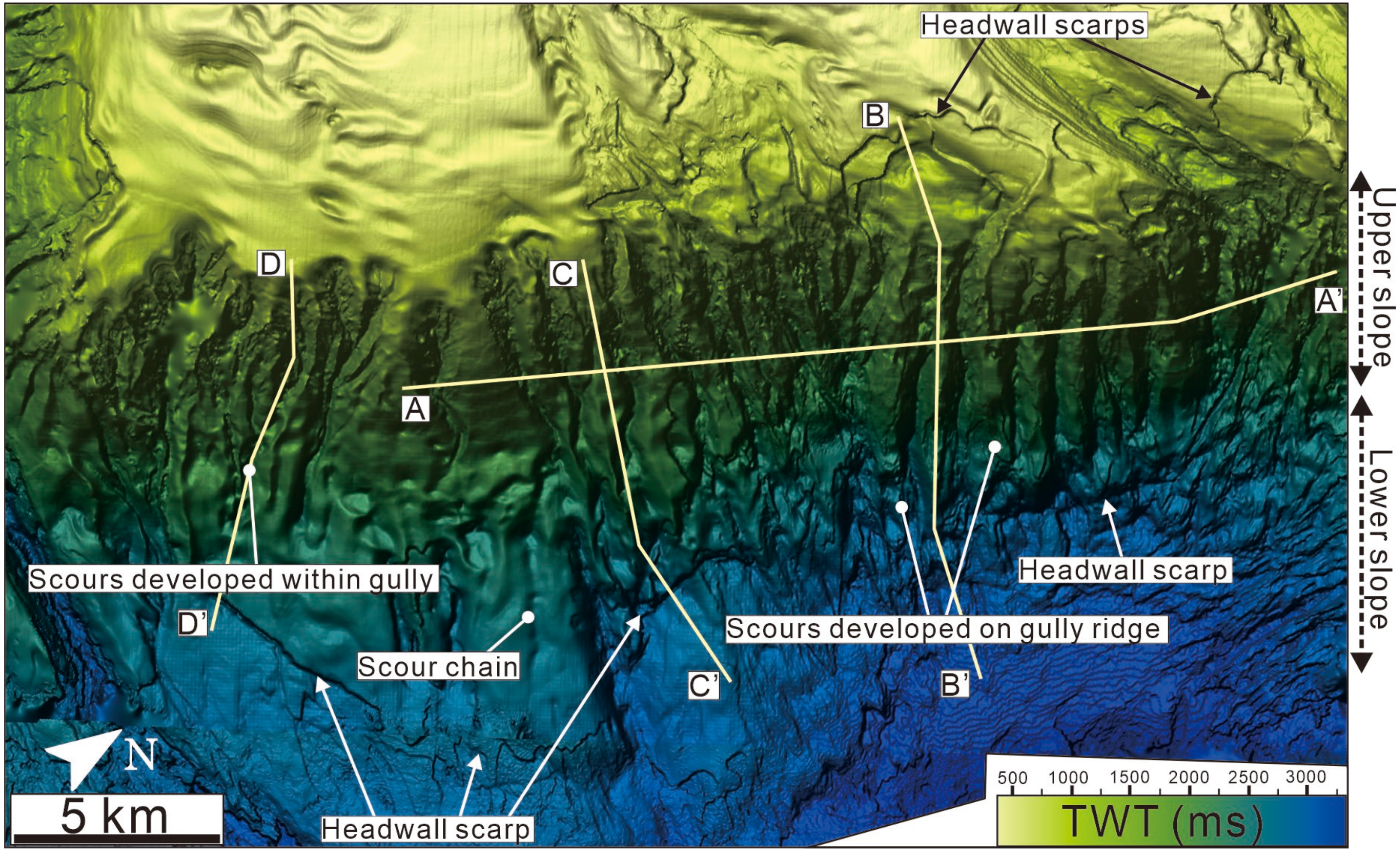

Headwall scarps
B
D
C
A'
A
Upper slope
Lower slope
Scours developed within gully
D'
Headwall scarp
Scours developed on gully ridge
Scour chain
C'
B'
N
5 km
Headwall scarp
500 1000 1500 2000 2500 3000
TWT (ms)

Figure 7

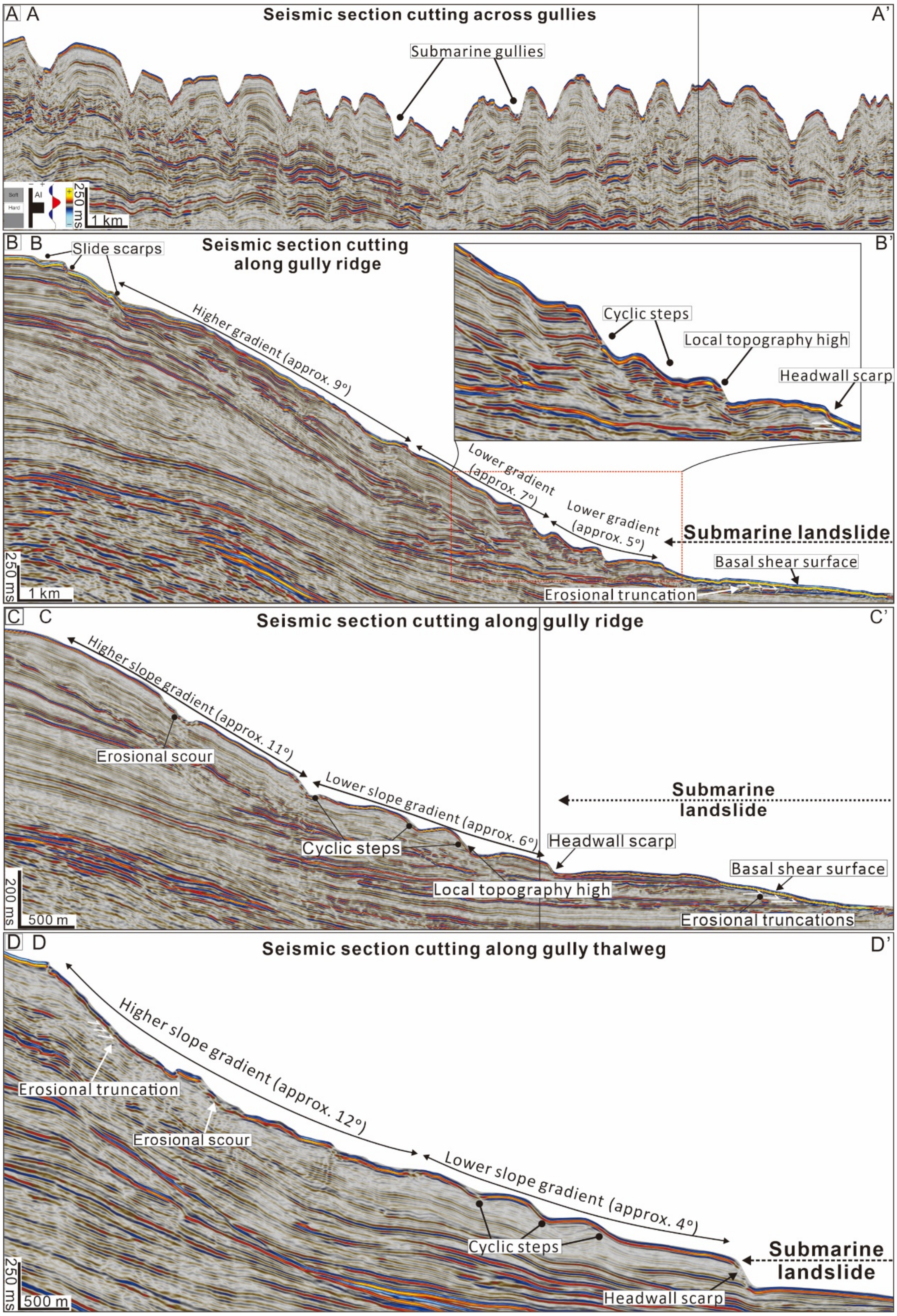

A A
Seismic section cutting across gullies
A'
Submarine gullies
Soft
Hard
AI
250 ms
1 km
B B
Slide scarps
Seismic section cutting
along gully ridge
B'
Higher gradient (approx. 9°)
Cyclic steps
Local topography high
Headwall scarp
Lower gradient
(approx. 7°)
Lower gradient
(approx. 5°)
Submarine landslide
Basal shear surface
Erosional truncation
250 ms
1 km
C C
Seismic section cutting along gully ridge
C'
Higher slope gradient (approx. 11°)
Erosional scour
Lower slope gradient (approx. 6°)
Submarine
landslide
Headwall scarp
Cyclic steps
Basal shear surface
Local topography high
Erosional truncations
200 ms
500 m
D D
Seismic section cutting along gully thalweg
D'
Higher slope gradient (approx. 12°)
Erosional truncation
Erosional scour
Lower slope gradient (approx. 4°)
Cyclic steps
Submarine
landslide
Headwall scarp
250 ms
500 m

Figure 8

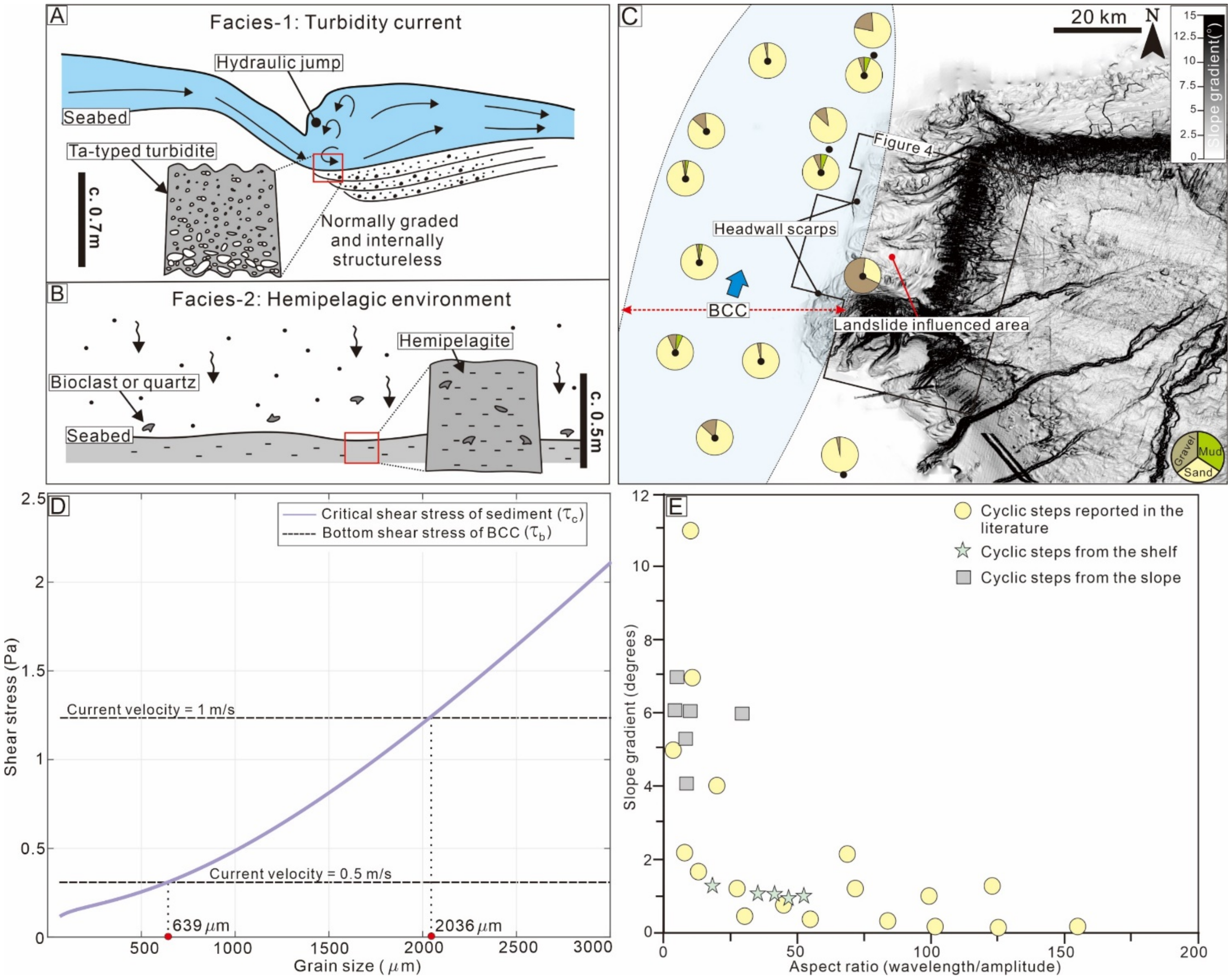

A
Facies-1: Turbidity current
Hydraulic jump
Seabed
Ta-typed turbidite
c. 0.7m
Normally graded and internally structureless
B
Facies-2: Hemipelagic environment
Hemipelagite
Bioclast or quartz
Seabed
c. 0.5m
C
20 km
N
Slope gradient(°)
Figure 4
Headwall scarps
BCC
Landslide influenced area
Gravel
Mud
Sand
D
Critical shear stress of sediment (τ_c)
Bottom shear stress of BCC (τ_b)
Shear stress (Pa)
Current velocity = 1 m/s
Current velocity = 0.5 m/s
639 μm
2036 μm
Grain size (μm)
E
Cyclic steps reported in the literature
Cyclic steps from the shelf
Cyclic steps from the slope
Slope gradient (degrees)
Aspect ratio (wavelength/amplitude)

Figure 9

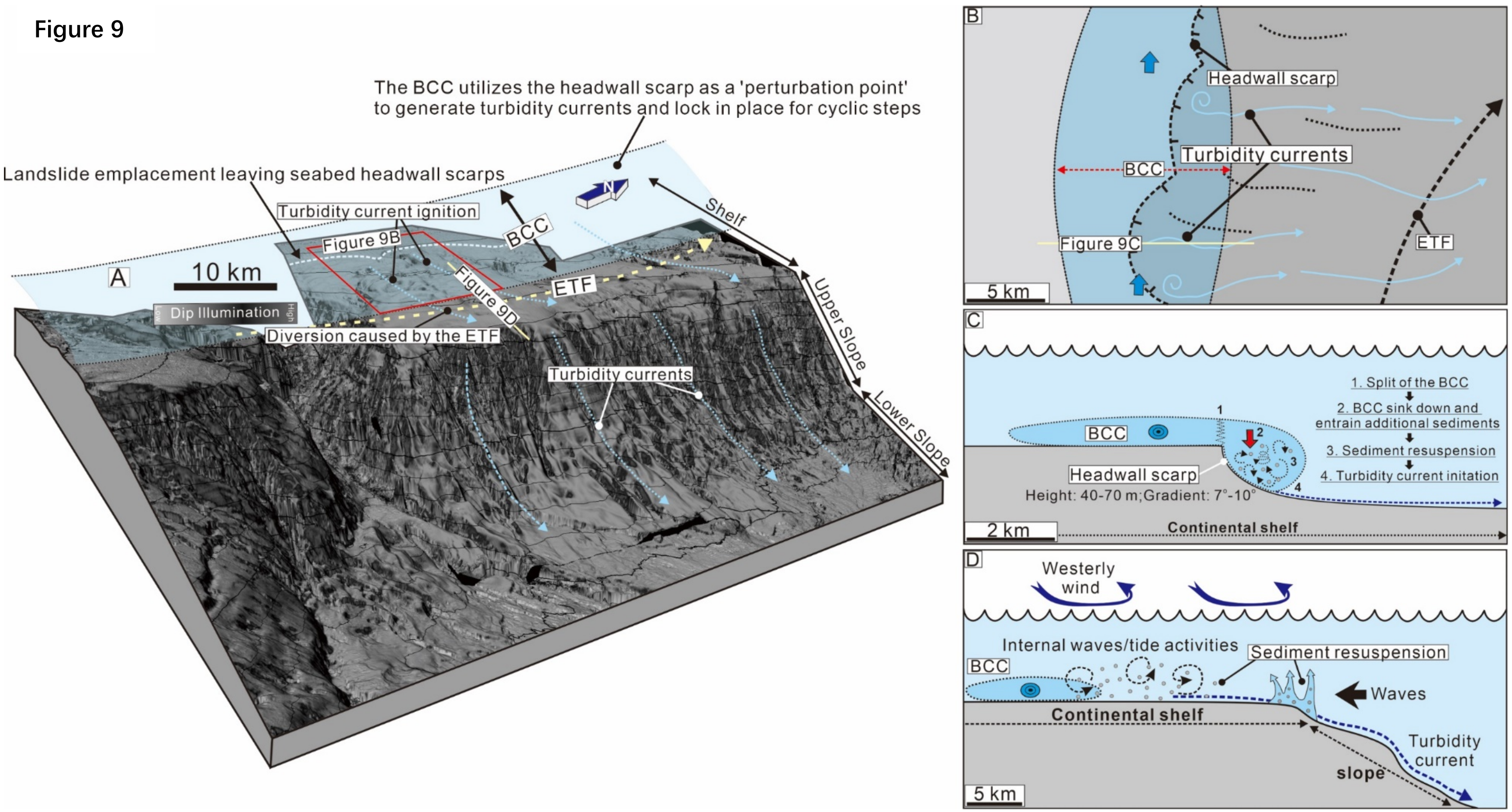

The BCC utilizes the headwall scarp as a 'perturbation point'
to generate turbidity currents and lock in place for cyclic steps
Landslide emplacement leaving seabed headwall scarps
Turbidity current ignition
Figure 9B
BCC
N
Shelf
A
10 km
Dip Illumination
ETF
Figure 9D
Diversion caused by the ETF
Upper Slope
Lower Slope
Turbidity currents
B
Headwall scarp
Turbidity currents
BCC
Figure 9C
ETF
5 km
C
1. Split of the BCC
2. BCC sink down and
entrain additional sediments
3. Sediment resuspension
4. Turbidity current initation
BCC
Headwall scarp
Height: 40-70 m;Gradient: 7°-10°
2 km
Continental shelf
D
Westerly
wind
Internal waves/tide activities
Sediment resuspension
BCC
Waves
Continental shelf
Turbidity
current
slope
5 km

Figure 10

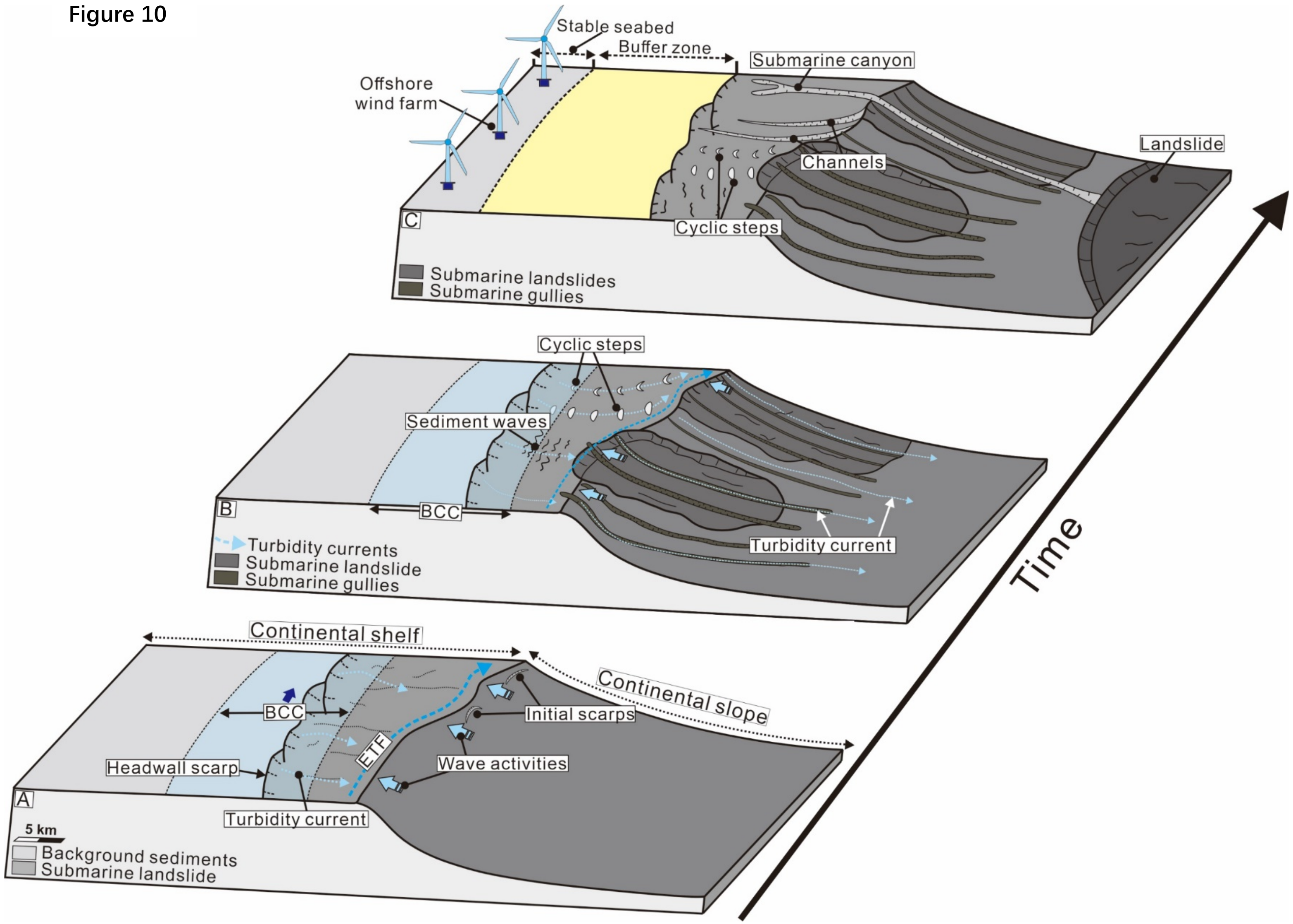

Stable seabed
Buffer zone
Offshore wind farm
Submarine canyon
Channels
Landslide
Cyclic steps
C
Submarine landslides
Submarine gullies
Cyclic steps
Sediment waves
BCC
B
Turbidity currents
Submarine landslide
Submarine gullies
Turbidity current
Time
Continental shelf
Continental slope
BCC
ETF
Initial scarps
Wave activities
Headwall scarp
Turbidity current
A
5 km
Background sediments
Submarine landslide